

Rabacus: A Python Package for Analytic Cosmological Radiative Transfer Calculations

Gabriel Altay^a, John H. Wise^a

^a*Center for Relativistic Astrophysics, Georgia Institute of Technology, 837 State Street, Atlanta, GA, 30332, USA*

Abstract

We describe **RABACUS**, a Python package for calculating the transfer of hydrogen ionizing radiation in simplified geometries relevant to astronomy and cosmology. We present example solutions for three specific cases: 1) a semi-infinite slab gas distribution in a homogeneous isotropic background, 2) a spherically symmetric gas distribution with a point source at the center, and 3) a spherically symmetric gas distribution in a homogeneous isotropic background. All problems can accommodate arbitrary spectra and density profiles as input. The solutions include a treatment of both hydrogen and helium, a self-consistent calculation of equilibrium temperatures, and the transfer of recombination radiation. The core routines are written in Fortran 90 and then wrapped in Python leading to execution speeds thousands of times faster than equivalent routines written in pure Python. In addition, all variables have associated units for ease of analysis. The software is part of the Python Package Index and the source code is available on Bitbucket at <https://bitbucket.org/galtay/rabacus>. In addition, installation instructions and a detailed users guide are available at <http://pythonhosted.org/rabacus>.

Keywords: radiative transfer, methods: numerical, Open-source software

1. Introduction

The transport of radiation is central to model building in astronomy and cosmology, yet few closed form solutions exist even in highly symmetric situations. In this work we describe **RABACUS**, a Python package for calculating equilibrium ionization and temperature states for well posed radiative transfer problems in planar or spherical geometries.

There is a long history of similar numerical approaches in the field of photon dominated regions or photo-dissociation regions (PDRs, see Hollenbach and Tielens, 1999; Röllig et al., 2007, for reviews). PDRs are usually defined as regions of the interstellar medium in which far ultraviolet photons with energies between 6 and 13.6 eV dominate the thermal and chemical dynamics. Typical densities and temperatures are $n_{\text{H}} \gtrsim 10 \text{ cm}^{-3}$ and $T \lesssim 5000 \text{ K}$. As the main goal of PDR codes is the calculation of emission spectra, they typically include large chemical networks and take account of many line excitation processes.

The goal of **RABACUS** is to provide a similar tool that is optimized for the transfer of hydrogen ionizing radiation through cosmological scale systems. Common applications include quasar absorption systems (Wolfe et al., 2005; Meiksin, 2009), the evaporation of mini-halos during reionization (Shapiro et al., 2004), and Strömgren spheres (Strömgren, 1939). Typical densities and temperatures in these regions are $n_{\text{H}} \lesssim 10^{-1} \text{ cm}^{-3}$ and $T \gtrsim 8000 \text{ K}$. This allows us to consider a compact chemical network consisting of hydrogen and helium and limits the list of physical processes that dominate the dynamics to photo-ionization, photo-heating, collisional ionization, collisional excitation, recombination, free-free radiation, Compton scattering, and Hubble expansion.

The density and temperature regime treated by **RABACUS** es-

entially excludes the cold inter-stellar medium phase of gas where molecules and dust begin to play an important role in the thermal and chemical state of hydrogen and helium. However, cooling from metal line emission can play an important role in diffuse enriched gas (e.g. Wiersma et al., 2009). Metal line cooling is not treated by **RABACUS**. However, its effect on hydrogen and helium can be approximated by first calculating the equilibrium temperature of a system without metals and then running iso-thermal models with lower temperatures.

Photo-ionization and heating rates are calculated in **RABACUS** using a multi frequency reverse ray tracing technique (Altay and Theuns, 2013). In cases of planar geometry this is simply a matter of evaluating exponential integrals, but in the case of spherical geometries embedded in isotropic radiation backgrounds, ray casting is used. This allows us to use the exact path length through each shell in our radiative transfer solutions.

The development of **RABACUS** has several purposes. One is the treatment of geometries and radiation fields that are not included in many popular codes in use today (for example plane parallel radiation incident from both sides of a slab or isotropic backgrounds incident on spherical geometries). In addition we wanted to use an object oriented approach coupled with a modern language with a large user base and fully developed graphical libraries. In addition, we wanted to make the isolation of physical processes convenient. We give special attention to physical processes that are most often treated in an approximate way in cosmological hydrodynamic simulations: 1) the spectral shape of the ionizing background, 2) the effect of helium on spectral hardening and hydrogen ionization profiles, 3) the effect of equilibrium temperatures vs. fixed temperatures, and 4) the effect of using the on-the-spot approximation vs. calculating the transfer of recombination radiation (e.g. Altay et al.,

2011; McQuinn et al., 2011; Friedrich et al., 2012; Rahmati et al., 2013; Raićević et al., 2014).

We developed the Python package `RABACUS` with the goal of making these solutions both available and readily usable by the astrophysics community at large. To this end, our project is free, open source, and makes use of a high level programming language with a large user base and well supported graphics packages. `RABACUS` is available on the Python Package Index¹; the source code is available on Bitbucket², and a users guide is available through pythonhosted.org³. The software is released under the terms of the FreeBSD license⁴. While Python has many benefits, the fact that it is an interpreted language can make computationally intensive tasks slow compared to compiled codes. In order to circumvent this problem we implemented the core functionality of `RABACUS` in Fortran 90 and wrapped the resulting code in Python using the Numpy package `f2py`. In addition, all variables in `RABACUS` have units through use of the Quantities Python package⁵. This package will automatically be downloaded during installation. Comprehensive examples in the users guide cover the use of variables with units. The rest of this paper is organized as follows. In §2 we present our notation and review some basic physics. In §3 we discuss classes that represent sources of radiation. In §4 we describe the single zone solvers supplied by `RABACUS`. In §5-8 we discuss the geometric solvers, and in §9 we conclude.

2. Basic Physics and Notation

In this section we review the physics governing the temperature and ionization state of cosmological gas. We will consider the number density of six species and indicate ionization states using Roman numerals $\{ n_{\text{HI}}, n_{\text{HII}}, n_{\text{HeI}}, n_{\text{HeII}}, n_{\text{HeIII}}, n_e \}$. The free electron number density is related to the other species as,

$$n_e = n_{\text{HII}} + n_{\text{HeII}} + 2n_{\text{HeIII}} \quad (1)$$

and the mass fraction of helium is given as,

$$Y \equiv \frac{4n_{\text{He}}}{n_{\text{H}} + 4n_{\text{He}}}, \quad \frac{n_{\text{He}}}{n_{\text{H}}} = \frac{Y}{4(1-Y)} \quad (2)$$

In what follows, we make use of the following notation,

$$\begin{aligned} x_{\text{HI}} &\equiv \frac{n_{\text{HI}}}{n_{\text{H}}}, & x_{\text{HII}} &\equiv \frac{n_{\text{HII}}}{n_{\text{H}}}, & x_e &\equiv \frac{n_e}{n_e^{\text{max}}}, \\ x_{\text{HeI}} &\equiv \frac{n_{\text{HeI}}}{n_{\text{He}}}, & x_{\text{HeII}} &\equiv \frac{n_{\text{HeII}}}{n_{\text{He}}}, & x_{\text{HeIII}} &\equiv \frac{n_{\text{HeIII}}}{n_{\text{He}}} \end{aligned} \quad (3)$$

where the electron fraction, x_e , is the ratio of the number density of electrons and the maximum possible number density of electrons,

$$\begin{aligned} n_e &= x_{\text{HII}}n_{\text{H}} + (x_{\text{HeII}} + 2x_{\text{HeIII}})n_{\text{He}} \\ &= \left[x_{\text{HII}} + \frac{Y(x_{\text{HeII}} + 2x_{\text{HeIII}})}{4(1-Y)} \right] n_{\text{H}} \end{aligned} \quad (4)$$

$$n_e^{\text{max}} = n_{\text{H}} + 2n_{\text{He}} = \left[1 + \frac{Y}{2(1-Y)} \right] n_{\text{H}}. \quad (5)$$

2.1. Ionization Evolution

Considering the processes of photo-ionization, collisional ionization, and recombination, the coupled evolution equations for the ionization fractions take the following form,

$$\begin{aligned} \frac{dx_{\text{HI}}}{dt} &= -(\Gamma_{\text{HI}} + C_{\text{HI}}n_e)x_{\text{HI}} + R_{\text{HII}}n_en_{\text{HII}} \\ \frac{dx_{\text{HII}}}{dt} &= -\frac{dx_{\text{HI}}}{dt} \end{aligned} \quad (6)$$

$$\begin{aligned} \frac{dx_{\text{HeI}}}{dt} &= -(\Gamma_{\text{HeI}} + C_{\text{HeI}}n_e)x_{\text{HeI}} + R_{\text{HeII}}n_en_{\text{HeII}} \\ \frac{dx_{\text{HeII}}}{dt} &= -\frac{dx_{\text{HeI}}}{dt} - \frac{dx_{\text{HeIII}}}{dt} \\ \frac{dx_{\text{HeIII}}}{dt} &= (\Gamma_{\text{HeII}} + C_{\text{HeII}}n_e)x_{\text{HeII}} - R_{\text{HeIII}}n_en_{\text{HeIII}} \end{aligned} \quad (7)$$

where the Γ 's represent photo-ionization rates, the C 's collisional ionization rates, and the R 's recombination rates. Collisional ionization and recombination rates have a non-trivial dependence on temperature and `RABACUS` provides a simple interface to load the rate fits presented in Hui and Gnedin (1997). Photo-ionization rates depend on the spectrum of ionizing radiation.

$$\begin{aligned} \Gamma_{\text{HI}} &= c \int_{\nu_{\text{HI}}^{\text{th}}}^{\infty} \frac{u_{\nu}\sigma_{\text{HI}}}{h\nu} \exp(-\tau_{\nu})d\nu \\ \Gamma_{\text{HeI}} &= c \int_{\nu_{\text{HeI}}^{\text{th}}}^{\infty} \frac{u_{\nu}\sigma_{\text{HeI}}}{h\nu} \exp(-\tau_{\nu})d\nu \\ \Gamma_{\text{HeII}} &= c \int_{\nu_{\text{HeII}}^{\text{th}}}^{\infty} \frac{u_{\nu}\sigma_{\text{HeII}}}{h\nu} \exp(-\tau_{\nu})d\nu \\ \tau_{\nu} &= N_{\text{HI}}\sigma_{\text{HI}} + N_{\text{HeI}}\sigma_{\text{HeI}} + N_{\text{HeII}}\sigma_{\text{HeII}} \end{aligned} \quad (8)$$

where u_{ν} is the energy density per unit frequency in radiation, τ_{ν} is the frequency dependent optical depth in all species, the N_x are column densities, the σ_x are frequency dependent photo-ionization cross sections, and the ν_x^{th} are ionization thresholds. Note that u_{ν} represents an optically thin quantity and $\exp(-\tau_{\nu})$ accounts for absorbing material between the source of radiation and the point at which the photo-ionization rate is being calculated.

`RABACUS` provides tools for the creation of spectra and access to the cross section fits of Verner et al. (1996). The variable u_{ν} serves to characterize the radiation field in a geometry independent way. It is related to more geometry specific characterizations as follows,

$$cu_{\nu} = 4\pi J_{\nu} = F_{\nu} = \frac{L_{\nu}}{4\pi r^2} \quad (9)$$

where J_{ν} is the angle averaged specific intensity, F_{ν} is the energy flux per unit frequency of a plane parallel source, L_{ν} is the energy luminosity per unit frequency of a point source and r is

¹<https://pypi.python.org/pypi/rabacus>

²<https://bitbucket.org/galtay/rabacus>

³<http://pythonhosted.org/rabacus>

⁴<http://opensource.org/licenses/BSD-2-Clause>

⁵<https://github.com/python-quantities/python-quantities>

the distance from the point source. It is sometimes convenient to group terms using the following notation,

$$\begin{aligned} \mathcal{I}_{\text{HI}} &= \Gamma_{\text{HI}} + C_{\text{HI}} n_e, & \mathcal{R}_{\text{HII}} &= R_{\text{HII}} n_e \\ \mathcal{I}_{\text{HeI}} &= \Gamma_{\text{HeI}} + C_{\text{HeI}} n_e, & \mathcal{R}_{\text{HeII}} &= R_{\text{HeII}} n_e \\ \mathcal{I}_{\text{HeII}} &= \Gamma_{\text{HeII}} + C_{\text{HeII}} n_e, & \mathcal{R}_{\text{HeIII}} &= R_{\text{HeIII}} n_e. \end{aligned} \quad (10)$$

However, it is important to keep in mind that n_e depends on the ionization fractions. Using this notation we can express these equations in matrix form,

$$\begin{aligned} \dot{\mathbf{x}}_{\text{H}} &= \mathbf{M}_{\text{H}} \mathbf{x}_{\text{H}} \\ \mathbf{M}_{\text{H}} &= \begin{pmatrix} -\mathcal{I}_{\text{HI}} & \mathcal{R}_{\text{HII}} \\ \mathcal{I}_{\text{HI}} & -\mathcal{R}_{\text{HII}} \end{pmatrix} \end{aligned} \quad (11)$$

$$\begin{aligned} \dot{\mathbf{x}}_{\text{He}} &= \mathbf{M}_{\text{He}} \mathbf{x}_{\text{He}} \\ \mathbf{M}_{\text{He}} &= \begin{pmatrix} -\mathcal{I}_{\text{HeI}} & \mathcal{R}_{\text{HeII}} & 0 \\ \mathcal{I}_{\text{HeI}} & -(\mathcal{I}_{\text{HeII}} + \mathcal{R}_{\text{HeII}}) & \mathcal{R}_{\text{HeIII}} \\ 0 & \mathcal{I}_{\text{HeII}} & -\mathcal{R}_{\text{HeIII}} \end{pmatrix} \end{aligned} \quad (12)$$

2.2. Temperature Evolution

The evolution of gas internal energy u is governed by the following equation,

$$u = \frac{3}{2} k_b T (n_{\text{H}} + n_{\text{He}} + n_e) \quad (13)$$

$$\frac{du}{dt} = \mathcal{H} - \Lambda_c - 3Hk_b T (n_{\text{H}} + n_{\text{He}} + n_e) \quad (14)$$

The first term, \mathcal{H} , accounts for photo-heating, the second term, Λ_c , accounts for radiative cooling, and the final term is due to adiabatic cooling from Hubble expansion. The first two are always included in the `RABACUS` solvers, but the last is optional. The photo-heating term depends on the spectrum of the radiation field.

$$\begin{aligned} \epsilon_{\text{HI}} &= c \int_{\nu_{\text{HI}}^{\text{th}}}^{\infty} \frac{u_{\nu} \sigma_{\text{HI}}}{h\nu} (h\nu - h\nu_{\text{HI}}^{\text{th}}) \exp(-\tau_{\nu}) d\nu \\ \epsilon_{\text{HeI}} &= c \int_{\nu_{\text{HeI}}^{\text{th}}}^{\infty} \frac{u_{\nu} \sigma_{\text{HeI}}}{h\nu} (h\nu - h\nu_{\text{HeI}}^{\text{th}}) \exp(-\tau_{\nu}) d\nu \\ \epsilon_{\text{HeII}} &= c \int_{\nu_{\text{HeII}}^{\text{th}}}^{\infty} \frac{u_{\nu} \sigma_{\text{HeII}}}{h\nu} (h\nu - h\nu_{\text{HeII}}^{\text{th}}) \exp(-\tau_{\nu}) d\nu \\ \mathcal{H} &= \epsilon_{\text{HI}} n_{\text{HI}} + \epsilon_{\text{HeI}} n_{\text{HeI}} + \epsilon_{\text{HeII}} n_{\text{HeII}} \end{aligned} \quad (15)$$

We consider the following radiative cooling processes,

- Collisional Ionization Cooling (cic)
- Collisional Excitation Cooling (cec)
- Dielectronic Recombination Cooling (di)
- Radiative Recombination Cooling (re)
- Bremsstrahlung Cooling (br)
- Compton Heating/Cooling (cp)

Their contribution to the cooling function is calculated as follows,

$$\begin{aligned} \frac{\Lambda_c}{n_e} &= \Lambda_{\text{HI}}^{\text{cec}} n_{\text{HI}} + \Lambda_{\text{HeII}}^{\text{cec}} n_{\text{HeII}} + \Lambda_{\text{HeII}}^{\text{di}} n_{\text{HeII}} + \\ &\quad \Lambda_{\text{HI}}^{\text{cic}} n_{\text{HI}} + \Lambda_{\text{HeI}}^{\text{cic}} n_{\text{HeI}} + \Lambda_{\text{HeII}}^{\text{cic}} n_{\text{HeII}} + \\ &\quad \Lambda_{\text{HII}}^{\text{re}} n_{\text{HII}} + \Lambda_{\text{HeII}}^{\text{re}} n_{\text{HeII}} + \Lambda_{\text{HeIII}}^{\text{re}} n_{\text{HeIII}} + \\ &\quad \Lambda^{\text{br}} g_{\text{ff}} T^{1/2} (n_{\text{HII}} + n_{\text{HeII}} + 4n_{\text{HeIII}}) + \\ &\quad \Lambda^{\text{cp}} (1+z)^4 (T - T_{\text{cmb}}) \end{aligned} \quad (16)$$

The first nine terms are products of temperature dependent rates and ion number densities. The next term accounts for bremsstrahlung cooling and involves a Gaunt factor which we set to $g_{\text{ff}} = 1.1 + 0.34 \exp[-(5.5 - \log_{10} T)^{2/3}]$. The final term accounts for Compton cooling. The fits used in `RABACUS` for these rates are from Hui and Gnedin (1997).

3. Source Classes

There are three source classes available in `RABACUS` namely, `PointSource`, `PlaneSource`, and `BackgroundSource`. The sources are grouped by geometry due to the different kinds of integrals that need to be computed in order to calculate quantities like photo-ionization and photo-heating rates. All classes presented here take a common set of arguments when instantiated. The first two, `q_min` and `q_max` are floats equal to the minimum and maximum photon energies considered divided by Rydbergs. The third determines the shape of the spectrum and is a string chosen from the following list { `monochromatic`, `hm12`, `thermal`, `powerlaw`, `user` } where `hm12` is the spectral model from Haardt and Madau (2012) (HM12) and `user` is a user defined spectrum. Keyword arguments supply extra information if needed. For example, the effective temperature in the case of thermal spectra, the powerlaw index in the case of powerlaw spectra, or the redshift in the case of `hm12`. All source classes contain geometry specific normalization routines. For example, a point source can be normalized to produce a given luminosity in erg s^{-1} while a plane source can be normalized to produce a given flux in $\text{erg cm}^{-2} \text{ s}^{-1}$.

By default, if the range of energies requested spans the hydrogen and helium ionizing thresholds (i.e. if `q_min` ≤ 1 and `q_max` $\geq \nu_{\text{HeII}}^{\text{th}} / \nu_{\text{HI}}^{\text{th}} \approx 4$) then frequency averaged, or “grey”, photo-ionization cross sections will be calculated as follows,

$$\begin{aligned} \sigma_{\text{HI}}^{\text{grey}} &= \frac{\int_{\nu_{\text{HI}}^{\text{th}}}^{\nu_{\text{HeI}}^{\text{th}}} u_{\nu} \sigma_{\text{HI}} d\nu / \nu}{\int_{\nu_{\text{HI}}^{\text{th}}}^{\nu_{\text{HeI}}^{\text{th}}} u_{\nu} d\nu / \nu} \\ \sigma_{\text{HeI}}^{\text{grey}} &= \frac{\int_{\nu_{\text{HeI}}^{\text{th}}}^{\nu_{\text{HeII}}^{\text{th}}} u_{\nu} \sigma_{\text{HeI}} d\nu / \nu}{\int_{\nu_{\text{HeI}}^{\text{th}}}^{\nu_{\text{HeII}}^{\text{th}}} u_{\nu} d\nu / \nu} \\ \sigma_{\text{HeII}}^{\text{grey}} &= \frac{\int_{\nu_{\text{HeII}}^{\text{th}}}^{\nu_{\text{max}}} u_{\nu} \sigma_{\text{HeII}} d\nu / \nu}{\int_{\nu_{\text{HeII}}^{\text{th}}}^{\nu_{\text{max}}} u_{\nu} d\nu / \nu} \end{aligned} \quad (17)$$

where $\nu_{\max} = q_{\max} \times \nu_{\text{HI}}^{\text{th}}$, and q_{\max} is one of the arguments provided to the source class. This allows for implicit definitions of grey frequencies and energies,

$$\sigma_X(\nu_X^{\text{grey}}) = \sigma_X^{\text{grey}}, \quad E_X^{\text{grey}} = h\nu_X^{\text{grey}} \quad (18)$$

where X is one of $\{\text{HI}, \text{HeI}, \text{HeII}\}$. However, these quantities are calculated only as a convenience to the user. *Unless a monochromatic spectrum is specified, the geometric solvers provided by RABACUS, described in §5, perform multi-frequency radiative transfer.*

By default, all spectra are sampled at $N_\nu = 128$ photon energies logarithmically spaced between q_{\min} and q_{\max} . The variable N_ν can be passed into the source initialization routines to increase or decrease spectral resolution. All photo-ionization and photo-heating rates are calculated by performing discretized versions of the integrals in Eqs. 8 and 15. Photo-ionization cross-sections are calculated by evaluating the fitting functions of Verner et al. (1996) at the N_ν photon energies. User defined spectra are defined by providing the energy samples and spectral shape in tabulated form. In general, increasing the value of N_ν increases the accuracy of the integrations at the cost of longer computations.

4. Single Zone Solvers

The single zone solvers provide equilibrium solutions to Eqs. 6, 7, and 14. Three classes are provided by RABACUS to handle three types of equilibrium.

4.1. Collisional Equilibrium

The first case we consider is that of collisional equilibrium handled by the class `Solve_CE`. In this case, temperatures are fixed, photo-ionization rates are zero, and ionization fractions are found such that collisional ionizations balance recombinations. In this case, there are closed form solutions for the ionization fractions,

$$x_{\text{HI}}^{\text{ce}} = \frac{R_{\text{HI}}}{R_{\text{HI}} + C_{\text{HI}}}, \quad x_{\text{HII}}^{\text{ce}} = \frac{C_{\text{HI}}}{R_{\text{HI}} + C_{\text{HI}}} \quad (19)$$

$$\begin{aligned} x_{\text{HeI}}^{\text{ce}} &= \frac{R_{\text{HeII}} R_{\text{HeIII}}}{R_{\text{HeII}} R_{\text{HeIII}} + R_{\text{HeIII}} C_{\text{HeI}} + C_{\text{HeI}} C_{\text{HeII}}} \\ x_{\text{HeII}}^{\text{ce}} &= \frac{R_{\text{HeIII}} C_{\text{HeI}}}{R_{\text{HeII}} R_{\text{HeIII}} + R_{\text{HeIII}} C_{\text{HeI}} + C_{\text{HeI}} C_{\text{HeII}}} \\ x_{\text{HeIII}}^{\text{ce}} &= \frac{C_{\text{HeI}} C_{\text{HeII}}}{R_{\text{HeII}} R_{\text{HeIII}} + R_{\text{HeIII}} C_{\text{HeI}} + C_{\text{HeI}} C_{\text{HeII}}} \end{aligned} \quad (20)$$

These solutions also determine the minimum possible electron density for a given temperature, $n_e^{\min} = x_{\text{HI}}^{\text{ce}} n_{\text{H}} + (x_{\text{HeI}}^{\text{ce}} + 2x_{\text{HeIII}}^{\text{ce}}) n_{\text{He}}$.

4.2. Photo Collisional Equilibrium

The second case we consider is that of photo-collisional equilibrium handled by the class `Solve_PCE`. In this case, temperatures are fixed, photo-ionization rates are finite, and ionization fractions are found such that collisional and photo ionizations balance recombinations. In this case, implicit solutions for the ionization fractions are,

$$x_{\text{HI}} = \frac{R_{\text{HI}}}{R_{\text{HI}} + I_{\text{HI}}}, \quad x_{\text{HII}} = \frac{I_{\text{HI}}}{R_{\text{HI}} + I_{\text{HI}}} \quad (21)$$

$$\begin{aligned} x_{\text{HeI}} &= \frac{R_{\text{HeII}} R_{\text{HeIII}}}{R_{\text{HeII}} R_{\text{HeIII}} + R_{\text{HeIII}} I_{\text{HeI}} + I_{\text{HeI}} I_{\text{HeII}}} \\ x_{\text{HeII}} &= \frac{R_{\text{HeIII}} I_{\text{HeI}}}{R_{\text{HeII}} R_{\text{HeIII}} + R_{\text{HeIII}} I_{\text{HeI}} + I_{\text{HeI}} I_{\text{HeII}}} \\ x_{\text{HeIII}} &= \frac{I_{\text{HeI}} I_{\text{HeII}}}{R_{\text{HeII}} R_{\text{HeIII}} + R_{\text{HeIII}} I_{\text{HeI}} + I_{\text{HeI}} I_{\text{HeII}}} \end{aligned} \quad (22)$$

They are implicit solutions due to the factors of n_e on the right hand side. It is possible to eliminate the n_e yielding a univariate fourth order polynomial equation for each ionization fraction, however this yields solutions with thousands of terms. In addition, the floating point errors involved in numerically evaluating these solutions with fixed precision frequently produce imaginary components.

In RABACUS we use a robust iterative approach. It involves an initial guess for n_e using a closed form solution for the hydrogen ionization fraction (see §6.1). This allows for the evaluation of all ionization fractions using Eqs. 21 and 22. These are then used to re-calculate n_e using Eq. 4 which in turn can be used to re-calculate the ionization fractions. This process is repeated until the amplitude of changes in n_e drops below a given tolerance. In most cases, the number of floating point operations for the iterative method will be less than the number required to evaluate the thousands of terms in the closed form solution. In addition, the initial guess for n_e is bounded between a maximum value of $n_e^{\max} = n_{\text{H}} + 2n_{\text{He}}$ and a minimum value given by collisional ionization equilibrium.

4.3. Photo Collisional Thermal Equilibrium

The third case we consider is that of photo-collisional-thermal equilibrium handled by the class `Solve_PCTE`. In this case, ionization fractions are found such that collisional and photo ionizations balance recombinations, and a temperature is found such that cooling balances heating. As described above, we use an iterative technique to find solutions. First a temperature is guessed then photo-collisional equilibrium is found at that temperature. Next, heating and cooling rates are calculated using the ionization fractions. If the heating rate is greater than the cooling rate, the temperature is increased and vice versa. This procedure is iterated until the heating rate is within a given tolerance of the cooling rate. The range of temperatures to search can be defined by the user but defaults to $T_{\min} = 7.5 \times 10^3$ K and $T_{\max} = 10^5$ K. The initial temperature guess is $\log T = (\log T_{\min} + \log T_{\max})/2$.

5. Geometric Solver Arguments

In the next two sections we present the geometric solver classes available in `RABACUS` and compare our solutions to those in the literature. These classes take a common set of arguments when instantiated. The first, `Edges`, defines the gas geometry. We focus on two geometries: spheres and semi-infinite slabs. Spherical gas distributions are centered on the origin and discretized into spherical layers separated by infinitesimally thin spherical shells. In this case, `Edges` is an array of radial distances indicating the position of each shell and typically has zero as the first element and the radius of the sphere as the last element. Slab gas distributions are discretized into rectilinear layers separated by infinitesimally thin planes. In this case, `Edges` is an array of distances indicating the position of each plane relative to the surface of the slab and typically has zero as the first element and the thickness of the slab as the last element. For N discrete layers, `Edges` will have $N+1$ entries. The next three arguments, `T`, `nH`, `nHe`, are arrays of length N describing the temperature, number density of hydrogen and number density of helium in each layer.

6. Slab Solvers

`RABACUS` has three slab classes: `SlabPln` which models plane parallel radiation incident from one side; `Slab2Pln` which models plane parallel radiation incident from both sides; and `Slab2Bgnd` which models a slab in a uniform isotropic background. Our first goal is to validate the `RABACUS` slab solver using a closed form solution in the case of monochromatic radiation and uniform density and temperature. Afterward, we demonstrate the effects of polychromatic spectra, temperature evolution, and recombination radiation.

To begin, we create two plane parallel radiation sources using the `PlaneSource` class. The first has a spectrum taken from the cosmological UV background model of Haardt and Madau (2012) (HM12) at $z = 3$ between 1 and 400 Rydbergs. We then use the neutral hydrogen grey energy (see Eq. 18) to create a monochromatic instance of `PlaneSource` and normalize it such that it has the same hydrogen photo-ionization rate as the polychromatic instance of `PlaneSource`. This results in a source with photons of energy 16.8 eV, a photon flux of $2.31 \times 10^5 \text{ cm}^{-2} \text{ s}^{-1}$, and a hydrogen photo-ionization rate of $\Gamma_{\text{H}} = 8.27 \times 10^{-13} \text{ s}^{-1}$. We then follow the same procedure using the `BackgroundSource` class. This produces four source objects (a pair of monochromatic sources and a pair of polychromatic sources used to find the grey energies) we can pass to the geometric solvers.

6.1. Plane Parallel Closed Form Solution

In the case of monochromatic plane parallel radiation incident from one side onto a pure hydrogen slab with uniform density and temperature, there is a closed form solution describing the ionization profile if the on-the-spot approximation is used (see the Appendix of Altay and Theuns, 2013),

$$zn_{\text{H}}\sigma = \left(\frac{1}{x_{\text{H}}^0} - \frac{1}{x_{\text{H}}} \right) + \ln \left[\frac{x_{\text{H}}(1 - x_{\text{H}}^0)}{x_{\text{H}}^0(1 - x_{\text{H}})} \right] + \frac{1}{x_{\text{H}}^{\text{ce}}} \ln \left[\frac{x_{\text{H}}(x_{\text{H}}^{\text{ce}} - x_{\text{H}}^0)}{x_{\text{H}}^0(x_{\text{H}}^{\text{ce}} - x_{\text{H}})} \right] \quad (23)$$

where z is depth into the slab, σ is the hydrogen photo-ionization cross-section at the monochromatic frequency considered, x_{H}^0 is the neutral fraction at the surface of the slab, and x_{H}^{ce} is the neutral fraction in collisional equilibrium at the fixed temperature of the slab. Note that this is an inverse solution in the sense that it provides depth into the slab as a function of neutral fraction. However, it allows the full ionization profile to be mapped out by plugging in values of x_{H} between the two extremes x_{H}^0 and x_{H}^{ce} . Eq. 19 is a closed form solution for x_{H}^{ce} . There is also a closed form solution for x_{H}^0 ,

$$x_{\text{H}}^0 = \frac{-B - (B^2 - 4AC)^{1/2}}{2A} \quad (24)$$

The coefficients in this quadratic solution are,

$$\begin{aligned} A &= (R_{\text{H}} + C_{\text{H}})n_{\text{H}} \\ B &= -[\Gamma_{\text{H}}^0 + R_{\text{H}}n_{\text{H}} + A(1 + y)] \\ C &= R_{\text{H}}n_{\text{H}}(1 + y) \end{aligned} \quad (25)$$

where y represents the contribution to free electrons from elements other than hydrogen, $n_{\text{e}} = (x_{\text{H}} + y)n_{\text{H}}$, and Γ_{H}^0 is the photo-ionization rate at the surface of the slab (Altay and Theuns, 2013).

To generate an appropriate slab model in `RABACUS`, we use the `Cosmology` class to calculate the critical density of hydrogen at $z = 3$ using the Planck cosmological parameters (Planck Collaboration et al., 2013) and then calculate the Jeans length (assuming a mean molecular weight $\mu = 1$) for gas at 10^4 K and $\Delta = 2200$ times the critical density. The value for Δ was arbitrarily chosen to produce a small neutral region in the slab and results in a length of $L = 4.17 \text{ kpc}$ and number densities of $n_{\text{H}} = 8.61 \times 10^{-3} \text{ cm}^{-3}$ and $n_{\text{He}} = 7.09 \times 10^{-4} \text{ cm}^{-3}$.

In Fig. 1 we show the closed form ($x_{\text{H}}^{\text{ana}}$, $x_{\text{H}}^{\text{ana}}$) and `RABACUS` solutions. We generated the `RABACUS` solution by passing the monochromatic plane source and the slab description to the `SlabPln` class. The maximum relative and absolute difference between the two solutions occurs near the ionization front but is always less than 7×10^{-3} and two orders of magnitude smaller than that over most of the length of the slab. This indicates that the basic machinery of the `RABACUS` solver is correct.

6.2. Isotropic Background, Recombination Radiation

In the previous section both the gas geometry and the radiation transport were one dimensional. In this section we discuss isotropic backgrounds and diffuse recombination radiation both of which introduce angular variables into the problem. The `Slab2Bgnd` class models an isotropic background incident onto a planar gas distribution. Here we describe the equations that are solved by `RABACUS` to account for both the background radiation and radiation from recombinations. We also note that

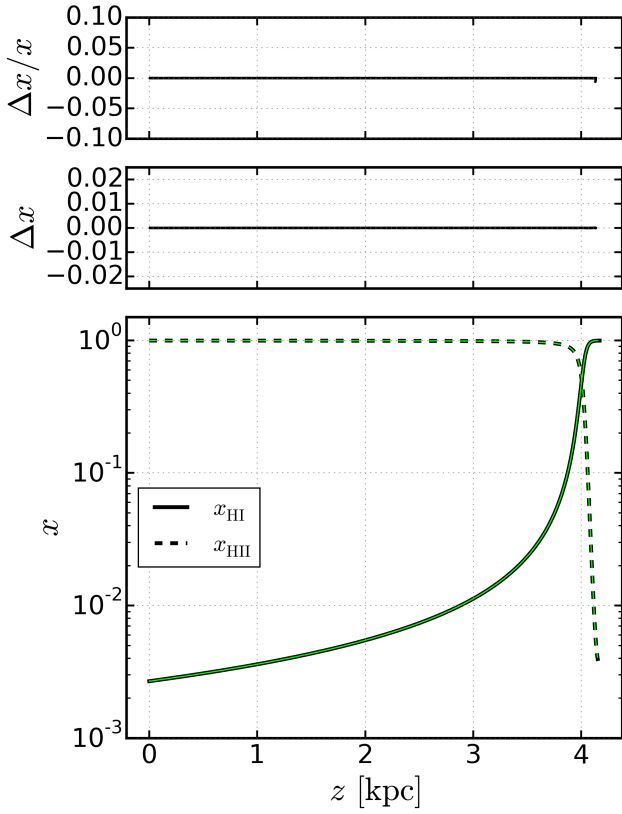


Figure 1: Ionization fractions for the closed form solution test described in section 6.1. In the lower panel we show ionization fractions from RABACUS (thick lines) and the closed form solution (thin lines). In the middle panel we show the absolute difference in ionization fractions $x^{\text{ana}} - \text{RABACUS}$. In the top panel we show the relative difference in ionization fractions $(x^{\text{ana}} - \text{RABACUS}) / \text{RABACUS}$. In the bottom panel, the RABACUS solution is shown in black while the analytic solution is shown in green.

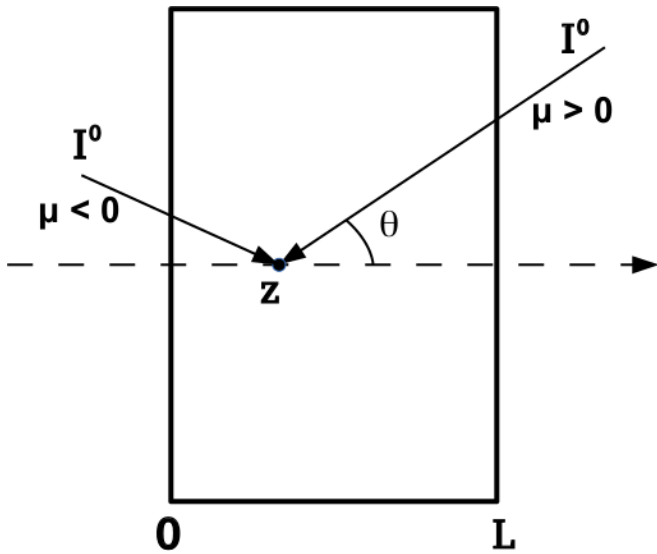


Figure 2: The geometry used in the SlabBgnd class.

recombination radiation can optionally be treated the same way in the SlabP1n and Slab2P1n classes.

The angle averaged specific intensity at any depth z (see Fig. 2) into the slab is,

$$J_\nu(z) = \frac{1}{4\pi} \int_0^{2\pi} d\phi \int_{-1}^1 d\mu I_\nu(z, \mu) \quad (26)$$

When considering a point at depth z , it is convenient to decompose the rays into those with negative z -components (I_ν^-) for which $\mu \equiv \cos \theta > 0$ and those with positive z -components (I_ν^+) for which $\mu < 0$. In addition, we will decompose the radiation into a component from the background itself (src) and a component from radiative recombinations in the slab (rec). Using this decomposition we can write,

$$I_\nu^{\text{src}+}(z, \mu) = I_\nu^0 \exp[-\tau(z)/|\mu|] \quad (27)$$

$$I_\nu^{\text{src}-}(z, \mu) = I_\nu^0 \exp[-\Delta\tau_{L,z}/\mu] \quad (28)$$

$$I_\nu^{\text{rec}+}(z, \mu) = \int_0^z \frac{dz'}{|\mu|} j_\nu(z') \exp[-\Delta\tau_{z,z'}/|\mu|] \quad (29)$$

$$I_\nu^{\text{rec}-}(z, \mu) = \int_z^L \frac{dz'}{\mu} j_\nu(z') \exp[-\Delta\tau_{z',z}/\mu] \quad (30)$$

where $\Delta\tau_{a,b} \equiv \tau(a) - \tau(b)$, $\tau(z')$ is the optical depth between $z = 0$ and $z = z'$ along a path perpendicular to the surface of the slab, j_ν is the emission coefficient for recombination radiation, and I_ν^0 is the un-attenuated isotropic background. The angle averaged specific intensity can now be written as,

$$J_\nu(z) = \frac{1}{2} \left[\int_{-1}^0 (I_\nu^{\text{src}+} + I_\nu^{\text{rec}+}) d\mu + \int_0^1 (I_\nu^{\text{src}-} + I_\nu^{\text{rec}-}) d\mu \right] \quad (31)$$

The angular integrals can be expressed in terms of the exponential integrals E_1 and E_2 ,

$$J_\nu^{\text{src}+}(z) = \frac{1}{2} \int_{-1}^0 I_\nu^{\text{src}+} d\mu = \frac{I_\nu^0}{2} E_2[\tau(z)] \quad (32)$$

$$J_\nu^{\text{src}-}(z) = \frac{1}{2} \int_0^1 I_\nu^{\text{src}-} d\mu = \frac{I_\nu^0}{2} E_2[\Delta\tau_{L,z}] \quad (33)$$

$$J_\nu^{\text{rec}+}(z) = \frac{1}{2} \int_{-1}^0 I_\nu^{\text{rec}+} d\mu = \frac{1}{2} \int_0^z dz' j_\nu(z') E_1(\Delta\tau_{z,z'}) \quad (34)$$

$$J_\nu^{\text{rec}-}(z) = \frac{1}{2} \int_0^1 I_\nu^{\text{rec}-} d\mu = \frac{1}{2} \int_z^L dz' j_\nu(z') E_1(\Delta\tau_{z',z}) \quad (35)$$

Combining all terms we get,

$$J_\nu(z) = \frac{I_\nu^0}{2} \{E_2[\tau(z)] + E_2[\Delta\tau_{L,z}]\} + \frac{1}{2} \int_0^L dz' j_\nu(z') E_1(|\Delta\tau_{z',z}|) \quad (36)$$

We account for recombination radiation from hydrogen and helium with monochromatic emission at the appropriate ionization threshold and calculate the emission coefficients as,

$$j_{\text{HII}} = \frac{R_{\text{HII}}^1 n_{\text{H}} x_{\text{HII}} n_e}{4\pi} \quad (37)$$

$$j_{\text{HeII}} = \frac{R_{\text{HeII}}^1 n_{\text{He}} x_{\text{HeII}} n_e}{4\pi}, \quad j_{\text{HeIII}} = \frac{R_{\text{HeIII}}^1 n_{\text{He}} x_{\text{HeIII}} n_e}{4\pi} \quad (38)$$

where the R_x^1 represent recombinations to the ground state of each ion. In practice, this rate is calculated by subtracting the case B fit from the case A fit. This neglects some helium recombinations that produce ionizing photons (see for example §3.1 in Altay et al., 2008) but makes for a more straightforward comparison to models which use case B rates only. Our treatment is similar to the models used in Faucher-Giguère et al. (2009) and Haardt and Madau (2012) except that we include the effects of collisional ionization.

6.3. Isolating Physical Processes

Having verified the basic functionality of RABACUS against a closed form solution, we now show the results of including more physical processes. All geometric solvers in RABACUS include the ability to treat polychromatic spectra, helium ionization, thermal balance, and the transfer of recombination radiation. We now use the slab geometry to produce five models which add these physical processes one at a time. For all of these examples we will use the `Slab2Bgnd` class which models a slab in an isotropic background of radiation. In general, plane parallel radiation will penetrate further into a slab than isotropic radiation. Therefore, we use a lower overdensity of $\Delta = 1800$ in this test. This leads to a slab of length $L = 4.61$ kpc and number densities $n_{\text{H}} = 7.04 \times 10^{-3} \text{ cm}^{-3}$ and $n_{\text{He}} = 5.80 \times 10^{-4} \text{ cm}^{-3}$. Although the temperature, and hence the Jeans length, will deviate from 10^4 K when we solve for thermal balance, we keep the slab size fixed for these tests. This results in a neutral hydrogen column density of $N_{\text{H}} = 5.67 \times 10^{18} \text{ cm}^{-2}$ for our most realistic model. These volume and column densities are typical for Lyman limit absorption systems. The five models we examine are,

grey_fixT_B monochromatic spectrum, fixed temperature, treats recombination photons by using case B rates

hm12_fixT_B adds full HM12 spectrum as opposed to the monochromatic grey approximation

hm12_evoT_B adds thermal balance as opposed to fixed temperatures

hm12_evoT_A same as **hm12_evoT_B** but with case A rates

hm12_evoT_rt uses case A recombination rates but adds the transfer of recombination photons from hydrogen and helium emitted isotropically from each layer

In Fig. 3 we show ionization and temperature profiles for all five models. Note that we have taken advantage of the symmetric geometry and only show half the slab. Above each profile panel we show the ratio of each model's predictions to those of **hm12_evoT_rt** (i.e. dex of difference in the bottom panel).

By comparing models **grey_fixT_B** and **hm12_fixT_B** we can isolate the effect of using the grey approximation. The monochromatic model is characterized by a fully neutral hydrogen core of approximately 1.5 kpc and sharp edges. Using the polychromatic spectrum smooths the hydrogen ionization profile and reduces the neutral hydrogen column density through

the slab, N_{H} , by a factor of 1.8. The monochromatic spectrum does not contain any helium ionizing photons and so a comparison between the helium ionization profiles is not well motivated.

By comparing models **hm12_fixT_B** and **hm12_evoT_B** we can isolate the effect of self-consistently calculating the temperature structure. The equilibrium temperature is greater than 10^4 K at all depths in the slab and peaks at 1.6×10^4 K at the edge. This produces both higher collisional ionization rates and lower recombination rates leading to fewer neutral hydrogen and helium atoms. This effect is compounded by the additional photons that can penetrate into the more ionized slab. Calculating the equilibrium temperatures lowers N_{H} by a factor of 11 and N_{He} by a factor of 6.3 while N_{HeII} is only affected at the five percent level.

By comparing models **hm12_evoT_B** and **hm12_evoT_A** we get a sense of the maximum variation possible due to recombination photons. In the case B model, recombination photons are emitted and absorbed in the same layer, while in the case A model all recombination photons escape the system. In model **hm12_evoT_rt** we calculate the transfer of recombination photons isotropically emitted from each layer. The rt and case A solutions agree at the optically thin surface of the slab. As depth increases, the rt solution diverges from the case A solution but always remains between the case A and case B solutions. This translates into a factor of 3.2 increase in both N_{H} and N_{He} relative to case B. These changes are larger than those that result from using a grey spectrum as opposed to a polychromatic one. The columns of singly and doubly ionized helium are only affected at the few percent level.

The fact that the rt solution does not converge to the case B result at any depth distinguishes the ionized slab model from models like the Strömgren sphere (see §7). The major difference is that Strömgren spheres necessarily have a neutral region enclosing the source of photons. Conservation of photons requires that all solutions agree at radii large enough where all photons have been absorbed. However, when the slab is not fully neutral at its center (as will be the case for Lyman limit systems as well as lower column density systems), the rt solution will differ from the case B solution at all points in the slab. In summary, the behavior of the most realistic solution here is not captured by either case A or case B approximations. In addition, the total column density in neutral hydrogen and helium differs between the models by at least a factor of 3 and at most a factor of 11.

7. Strömgren Sphere Solver

RABACUS has two sphere classes: `SphereStromgren` which models a point source at the center of a sphere and `SphereBgnd` which models a sphere placed in a uniform and isotropic background. There is no closed form solution that describes the ionization profile in either case, however solutions are readily found using numerical integration. In this section and the next we present the solutions of RABACUS and compare them to the results of the photo-ionization code CLOUDY version 13.03 last described in Ferland et al. (2013).

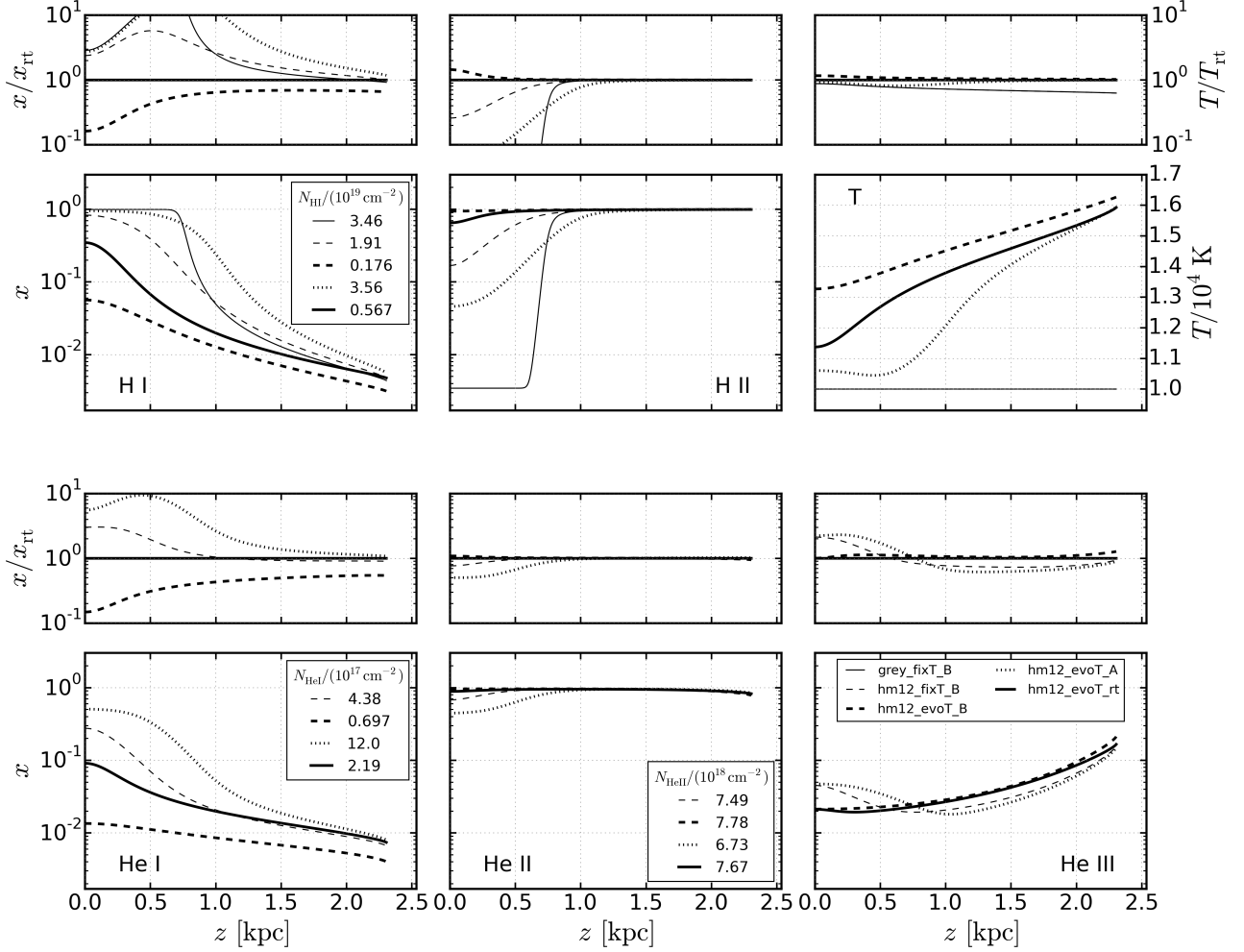


Figure 3: Ionization fraction and temperature profiles in five simple models of a Lyman limit system. Each panel shows the ionization fraction of one ion or the temperature. The five models considered are: 1) **grey_fixT_B** (thin solid) in which the grey approximation to the HM12 spectrum is used, the temperature is kept fixed, and recombinations are treated using case B rates, 2) **hm12_fixT_B** (thin dashed) in which the full HM12 spectrum is used, the temperature is kept fixed, and recombinations are treated using case B rates, 3) **hm12_evoT_B** (thick dashed) in which the full HM12 spectrum is used, equilibrium temperatures are calculated, and recombinations are treated using case B rates, 4) **hm12_evoT_A** (dotted) as in **hm12_evoT_B** but with case A recombination rates (i.e. recombination radiation is ignored) and 5) **hm12_evoT_rt** (thick solid) in which the full HM12 spectrum is used, equilibrium temperatures are calculated, recombination rates are case A, and recombinations are treated by calculating the transfer of radiation through the system. Above each profile we show the ratio of each model's prediction to those of **hm12_evoT_rt** (i.e. dex of difference in the profile panels). The scale in the top panels is a factor of ten in either direction.

We do not expect perfect agreement between the two codes for several reasons. First, `CLOUDY` makes use of a more detailed physical model including multi-level atoms and a large number of line transfer processes which are not included in `RABACUS`. Second, the convergence criteria for `CLOUDY` allow for a deviation from unity in the sum of the ionization fractions of a given element (for example $x_{\text{HI}} + x_{\text{HII}}$) at the level of 10^{-4} . Third, the atomic rates that determine the exact ionization and temperature structure in a parcel of gas are only known to a few significant digits at best and are not identical in the two codes. This is why we have tested `RABACUS` in previous sections against closed form analytic solutions. It follows that differences between `CLOUDY` and `RABACUS` should be considered a measure of uncertainty as opposed to an error in either code, both of which have been verified against analytic solutions.

The transfer of radiation from a central point source (ignoring recombination radiation for the moment) is a one-dimensional problem. This means the same techniques that we used in the case of plane parallel radiation incident on a slab geometry can be applied to the sphere as long as we include the inverse square geometric dilution of the radiation. In the following sections we verify the spherical solver in `RABACUS` using a simple test problem and then study the effects of temperature evolution, helium, and recombination radiation.

7.1. Pure Hydrogen, Fixed Temperature

We begin by examining Test 1 described in Iliev et al. (2006) which considers a pure hydrogen sphere of radius 6.6 kpc with uniform density, $n_{\text{H}} = 10^{-3} \text{ cm}^{-3}$, and temperature, $T = 10^4 \text{ K}$. The source has a photon luminosity of $L_{\text{n}} = 5.0 \times 10^{48}$ per second. The test specifies a monochromatic spectrum with all photons having energy 13.6 eV. However, all spectra in `CLOUDY` have a finite width and so creating a monochromatic spectrum at the Lyman limit produces some non-hydrogen ionizing photons. In order to make a clean comparison to `RABACUS` we instead use a monochromatic spectrum at 1.1 Ry or 15 eV. Recombination photons are treated by using the case B recombination rate (i.e. the on-the-spot approximation). In Figure 4 we present ionization profiles from both codes. The relative difference between the two solutions is typically less than one percent but can be a few percent near the ionization front.

7.2. Temperature Evolution

The second test from Iliev et al. (2006) allows for temperature evolution and includes a black body spectrum with effective temperature $T_{\text{eff}} = 10^5 \text{ K}$. We only consider photons with energy between 1 and 10 Rydbergs and normalize the spectrum such that the source emits $L_{\text{n}} = 5 \times 10^{48}$ photons per second. The temperature profile of the sphere is determined by balancing photo-heating and radiative cooling processes. We present the solutions from `RABACUS` and `CLOUDY` in Fig. 5. The relative difference in ionization fractions and temperature between the two codes for this test is on the order of a few percent except in the innermost quarter kpc. These differences coincide with the radius at which x_{HI} approaches the magnitude of the deviation from unity of the ionization fractions, $\delta_{\text{H}} = |1 - x_{\text{HI}} - x_{\text{HII}}|$, in the `CLOUDY` model.

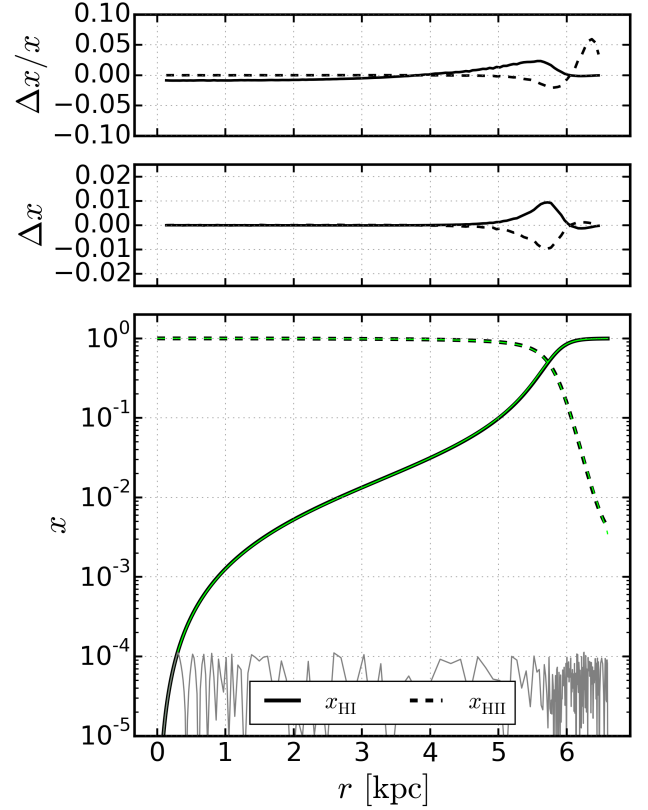


Figure 4: Ionization fractions for Test 1 of Iliev et al. (2006) (with 15 eV photons). In the lower panel we show ionization fractions from `RABACUS` (thick lines) and `CLOUDY` (thin lines). The deviation of the sum of the ionization fractions from unity ($\delta_{\text{H}} = |1 - x_{\text{HI}} - x_{\text{HII}}|$) in the `CLOUDY` model is shown as a thin grey line. In the middle panel we show the absolute difference in ionization fractions `CLOUDY` - `RABACUS`. In the top panel we show the relative difference in ionization fractions (`CLOUDY` - `RABACUS`) / `RABACUS`. In the bottom panel, the `RABACUS` solution is shown in black and the `CLOUDY` solution is shown in green.

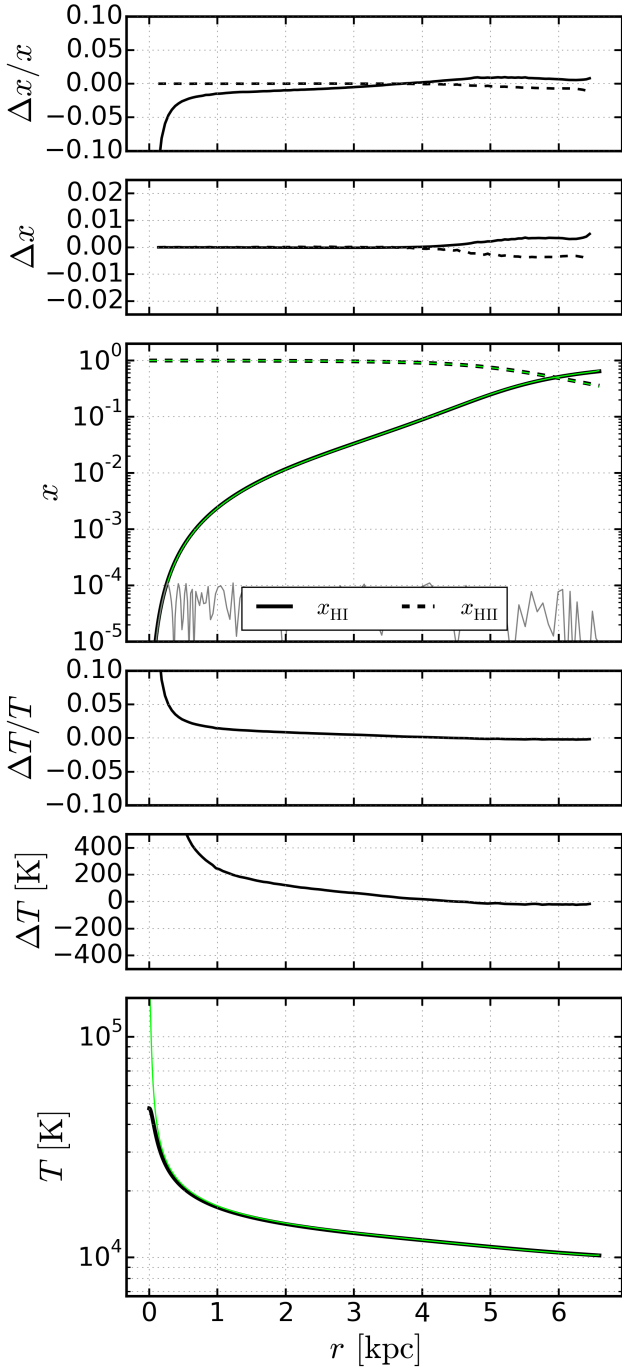


Figure 5: Ionization and temperature profiles for Test 2 of Iliev et al. (2006). In the upper three panels we show ionization fractions from RABACUS (thick black lines) and CLOUDY (thin green lines). The deviation of the sum of the ionization fractions from unity ($\delta_H = |1 - x_{\text{HI}} - x_{\text{HII}}|$) in the CLOUDY model is shown as a thin grey line. The top two panels show the absolute difference in ionization fractions, CLOUDY - RABACUS, and the relative difference in ionization fractions, (CLOUDY - RABACUS) / RABACUS. The bottom three panels show the same thing for temperature. The difference between the two codes in the temperature profile panel is only significant for the innermost quarter kpc. These differences coincide with the radius at which x_{HI} approaches δ_H in the CLOUDY model.

7.3. Inclusion of Helium

Friedrich et al. (2012) extend the spherically symmetric tests described in Iliev et al. (2006) to include a uniform helium density of $n_{\text{He}} = 8.7 \times 10^{-5} \text{ cm}^{-3}$ and increase the radius of the sphere to 20 kpc. To verify the treatment of helium in RABACUS we use a 10^5 K blackbody spectrum, case A recombination rates (i.e. ignore recombination radiation), and allow temperatures to vary as in the previous test. We consider photons with energy between 1 and 10 Rydbergs and normalize the spectrum such that the source emits $L_{\text{n}} = 5 \times 10^{48}$ photons per second. Except for the addition of temperature evolution, this is the same setup as Test 1 A in Friedrich et al. (2012). We use both RABACUS and CLOUDY to generate solutions and present the ionization and temperature profiles in Fig. 6. At small radii we see the same effect as in the previous test due to the neutral fractions approaching $\delta_H = |1 - x_{\text{HI}} - x_{\text{HII}}|$ and $\delta_{\text{He}} = |1 - x_{\text{HeI}} - x_{\text{HeII}} - x_{\text{HeIII}}|$. At larger radii, the relative differences in the hydrogen and helium neutral fractions are always less than 5%. In the case of the ionized species, the relative differences between ionization fractions in RABACUS and CLOUDY is less than 10% for most radii. However, for ionized hydrogen and doubly ionized helium, the differences can be greater. It is hard to determine the exact cause of these differences, but the most likely explanations are differences in the atomic rates used in the two codes and line processes in CLOUDY that are not included in RABACUS. The absolute difference between ionization fractions in the two codes is always less than 0.02.

7.4. Hydrogen Recombination Radiation

In the previous Strömgren sphere examples, we have either ignored recombination radiation (i.e. used case A rates) or treated it using the on-the-spot approximation (i.e. used case B rates). A more accurate treatment would allow photons produced via recombinations to travel some distance in the system before producing a photo-ionization. The outward only approximation is commonly used in analytic treatments of Strömgren spheres (e.g. Ritzerveld, 2005). In this approximation, all recombination photons are assumed to be emitted in the outward radial direction. This is equivalent to a situation in which half the photons are emitted radially inward and half radially outward *if* the optical depth seen by recombination photons interior to the emitting layer is zero. Raičević et al. (2014) examine the effects of isotropically transporting recombination radiation in the Strömgren sphere problem using the same physical setup as in Test 1 of Iliev et al. (2006). RABACUS includes options to treat the isotropic emission of recombination radiation as well as options to use the outward only approximation. In this section, we present solutions produced by RABACUS with isotropic transport of recombination radiation.

When radiation is not constrained to move in the radial direction, one must account for the angular dependence of the optical depth when calculating photo-ionization and photo-heating rates. In spherical geometries this angular dependence is restricted to a dependence on the polar angle $\mu = \cos \theta$. To calculate the transfer of recombination radiation, one must calculate

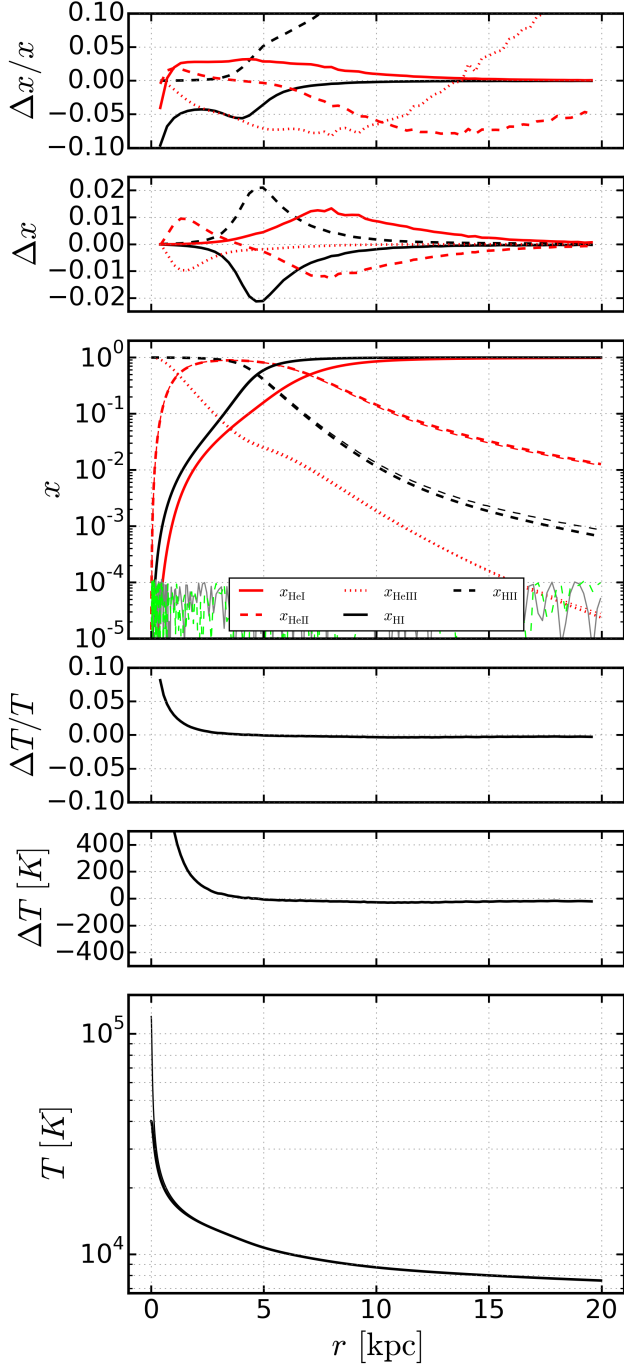


Figure 6: Ionization and temperature profiles for Test 1 A of Friedrich et al. (2012) with the addition of temperature evolution. In the upper three panels we show ionization fractions from RABACUS (thick lines) and CLOUDY (thin lines). The deviation of the sum of the ionization fractions from unity ($\delta_{\text{H}} = |1 - x_{\text{HI}} - x_{\text{HII}}|$ and $\delta_{\text{He}} = |1 - x_{\text{HeI}} - x_{\text{HeII}} - x_{\text{HeIII}}|$) in the CLOUDY model are shown as thin grey and green lines respectively. The top two panels show the absolute difference in ionization fractions, CLOUDY - RABACUS, and the relative difference in ionization fractions, (CLOUDY - RABACUS) / RABACUS. The lines from the two codes are only distinguishable for the ionized species at large radii. The bottom three panels show the same thing for temperature. The difference between the two codes in the temperature profile panel is only visible at small radii.

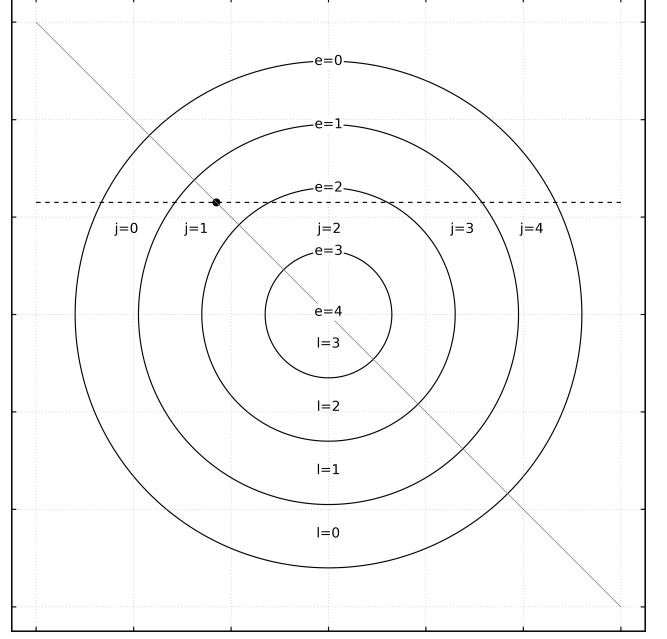


Figure 7: Illustration of ray tracing in spherical geometries. Because of symmetry, all rays (dashed line) can be rotated such that they are perpendicular to the vertical axis. We indicate the origin of the rays with a dot in the center of the $l = 1$ layer and the radial direction with a grey solid line. In the calculation of path length ds through each layer we label the edges (from large to small radii) with the integer e , the layers (from large to small radii) with the integer l and the ray segments (from left to right) with the integer j .

the optical depth through the sphere along N_μ directions for every layer. Each ray begins at the center of a layer and the directions, μ_i are chosen using Gauss-Legendre quadrature. The number of directions can be specified by the user but defaults to $N_\mu = 32$. We found that increasing or decreasing the number of angles by a factor of 2 had no effect on the tests presented here, however users should check convergence for each problem.

With the proper rotation, all rays can be made perpendicular to the vertical axis. In Fig. 7 we show two rays that originate from the layer $l = 1$. The first (extending to the left) represents a direction with $\mu_i = \cos \theta > 0$ while the second (extending to the right) represents a direction with $\mu_i = \cos \theta < 0$. We label the edges of the sphere (from large to small radii) with the integer e , the layers of the sphere (from large to small radii) with the integer l , and the segments of the ray (from left to right) with the integer j . Given a layer of origin and a direction μ_i , we first calculate the impact parameter b and the layer of closest approach l_b (e.g. $l_b = 2$ in Fig. 7). In addition we label the radius of each edge with the function $r_e(i)$. Given this information, the path length $ds(j)$ through segment j can be calculated as follows,

$$ds(j) = \begin{cases} \sqrt{r_e^2(j+1) - b^2} - \sqrt{r_e^2(j) - b^2} & \text{if } j < l_b, \\ 2\sqrt{r_e^2(j) - b^2} & \text{if } j = l_b, \\ \sqrt{r_e^2(k+1) - b^2} - \sqrt{r_e^2(k) - b^2} & \text{if } j > l_b. \end{cases} \quad (39)$$

$$k = l_b - |l_b - j| \quad (40)$$

When modeling an isotropic background external to the sphere, one adds the optical depth from each ray segment j between the ray origin and the surface of the sphere. This is then used to attenuate the incoming radiation. When modeling recombination radiation, emission from each layer is attenuated using the appropriate optical depth segments.

In the upper panel of Fig. 8 we show hydrogen ionization profiles when using case A recombination rates (i.e. ignoring recombination radiation), when using case B recombination rates (i.e. the on-the-spot approximation), and when transporting recombination radiation isotropically. As expected, the case A result produces the smallest ionized region. The case B result assumes that each recombination produces a local ionization and so produces a larger ionized region. When recombination photons are emitted isotropically, they travel through the low optical depths at small radii without being absorbed and the solution tracks the case A model. However, all photons are eventually absorbed in the Strömgen sphere problem and so the final radius of the Strömgen sphere must be the same as in the case B approximation due to photon conservation. This result does not hold for slab geometries which are optically thin at their center (see §6.3).

An instance of the `SphereStromgren` class has attributes that store photo-ionization rates due to both the central source and to diffuse recombination radiation. In the lower panels of Fig. 8 we show how these scale with radius. The diffuse field for the on-the-spot approximation is calculated using what we term the effective photo-ionization rate. In addition, to tracking the source and diffuse photo-ionization rates, `RABACUS` will define an effective photo-ionization rate, Γ^{eff} , for each ionized species if recombination photons are not being transported. The effective rates are defined for each layer to be those that would result in the same ionization fractions *if* case A recombination rates were used. By definition the effective photo-ionization rate is equal to the actual photo-ionization rate if case A rates are used. However, if case B rates are used, subtracting the actual photo-ionization rate from the effective photo-ionization rate leaves the diffuse photo-ionization rate. The on-the-spot approximation produces a constant ratio of approximately 0.6 between diffuse and central source photons. When ray tracing is used to follow the isotropic emission of recombination photons, their contribution peaks near a radius of 4 kpc on the flat part of the ionization profile and goes to zero at the center of the sphere. These results are consistent with the findings of Raičević et al. (2014).

7.5. Helium Recombination Radiation

Few papers have focused on the effects of diffuse radiation in the presence of hydrogen and helium (although see Cantalupo and Porciani, 2011). In `RABACUS`, we allow for the transport of radiation due to recombinations to the ground state for all ions. This allows for meaningful comparison to case A and case B approximations. In future versions of the code we will include ionizing photons produced by other processes such as

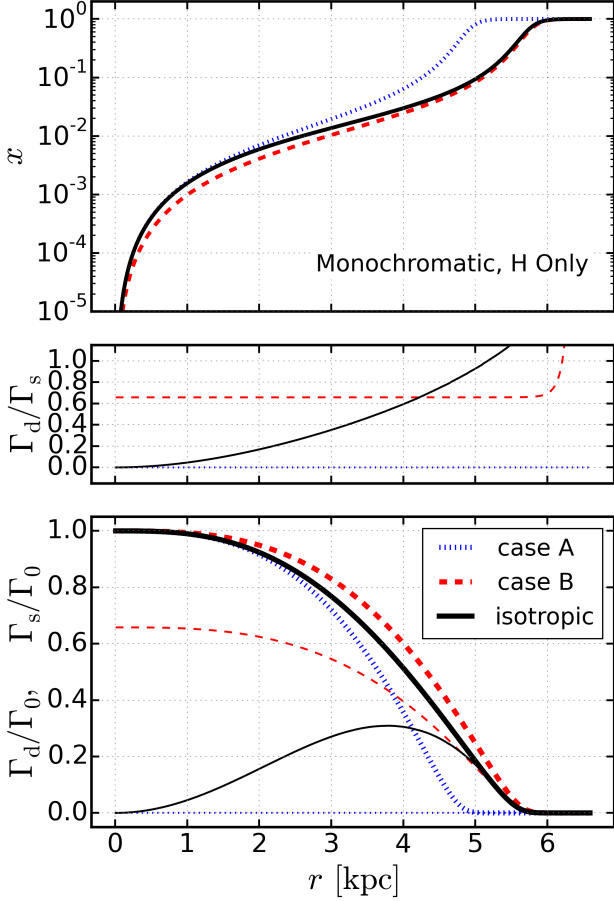


Figure 8: Results for the test described in Raičević et al. (2014). In the upper panel we show the neutral hydrogen fraction resulting from using case A rates (ignoring recombination radiation), using case B rates (using the on-the-spot approximation) and from transporting recombination radiation isotropically. In the lower panel we show photo-ionization rates due to the central source (thick lines) and due to recombination radiation (thin lines) all with geometric dilution scaled out. In the middle panel we show the ratio of diffuse to central source rates.

Balmer series recombinations, two photon processes, and secondary ionizations and heating from fast ($E > 100$ eV) electrons (Shull and van Steenberg, 1985; Furlanetto and Stoever, 2010).

To examine the effects of helium recombination photons we create a point source with a photon luminosity of $L_n = 10^{48}$ photons per second and a powerlaw spectrum with $L_\nu \propto \nu^{-\alpha}$ between 1 and 60 Rydbergs. Fig. 9 is analogous to Fig. 8 but for helium ionization profiles and photo-ionization rates. For isotropic transport of recombination photons we find that the diffuse photo-ionization rate for neutral helium is never greater than 0.2 of the direct source rate but peaks around 4 kpc for singly ionized helium as in the case of hydrogen. While the case B approximation is more accurate for the outer radii in our previous tests involving hydrogen, the case A approximation is more accurate for helium. This result is due to the fact that helium recombination photons are less effective at ionizing helium than hydrogen recombination photons are at ionizing hydrogen. In fact, the opacity seen by helium recombination photons comes mostly from neutral hydrogen. In addition, the higher energy and lower photo-ionization cross-section of helium recombination photons allow some to escape the system all together (see §Appendix A). However, we show in Fig. 10 that these results are sensitive to the steepness of the central source spectrum.

To illustrate the previous point, we calculate the ionization structure in the sphere using five powerlaw spectra with spectral slopes α evenly spaced between 0 and 4 all normalized to emit $L_n = 10^{48}$ photons per second. We present the results in Fig. 10. In general, steeper spectral slopes produce a larger ratio of low-energy to high-energy photons leading to an increased singly-ionized helium fraction at $r < 4$ kpc. This in turn leads to a higher rate of recombination for singly ionized helium and the increased importance of recombination radiation relative to central source photons for ionizing neutral helium in the inner region. As the spectrum flattens, diffuse radiation becomes decreasingly important for both neutral and singly ionized helium, however the effect is stronger for neutral helium. Furthermore, a flatter spectrum contains more high-energy photons than steeper spectra, which then doubly-ionize helium at a higher rate. However, the optical depth of its recombination radiation is small (see §Appendix A) and most of the diffuse radiation escapes from the system.

7.6. Isolating Physical Processes

As a final examination of the capabilities of the Sphere-Stromgren class we solve five models similar to those described in the slab geometry section (see §6.3) to gain some insight into the effects of different physical processes. The sphere we consider has a radius of 20 kpc and hydrogen and helium number densities of $n_H = 10^{-3} \text{ cm}^{-3}$ and $n_{He} = 8.7 \times 10^{-5} \text{ cm}^{-3}$. We consider a 10^5 K blackbody source and its grey approximation (17.8 eV) both normalized to emit 5×10^{48} photons per second. The polychromatic models are prefixed with **t1e5** as opposed to **hm12** to indicate this change in spectrum.

In Fig. 11 we show ionization and temperature profiles for all five models. Above each profile panel we show the ra-

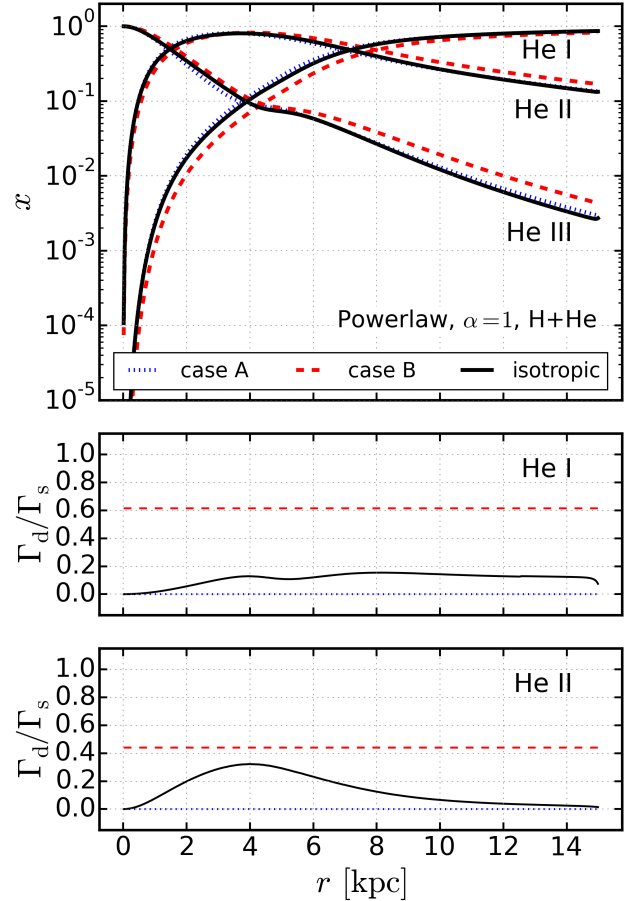


Figure 9: Results for a version of the test described in Raičević et al. (2014) extended to include helium. In the upper panel we show the ionization fractions for all three helium ions resulting from using case A rates (ignoring recombination radiation), using case B rates (using the on-the-spot approximation) and from transporting recombination radiation isotropically. In the lower panels we show the ratio of diffuse to central source photo-ionization rates.

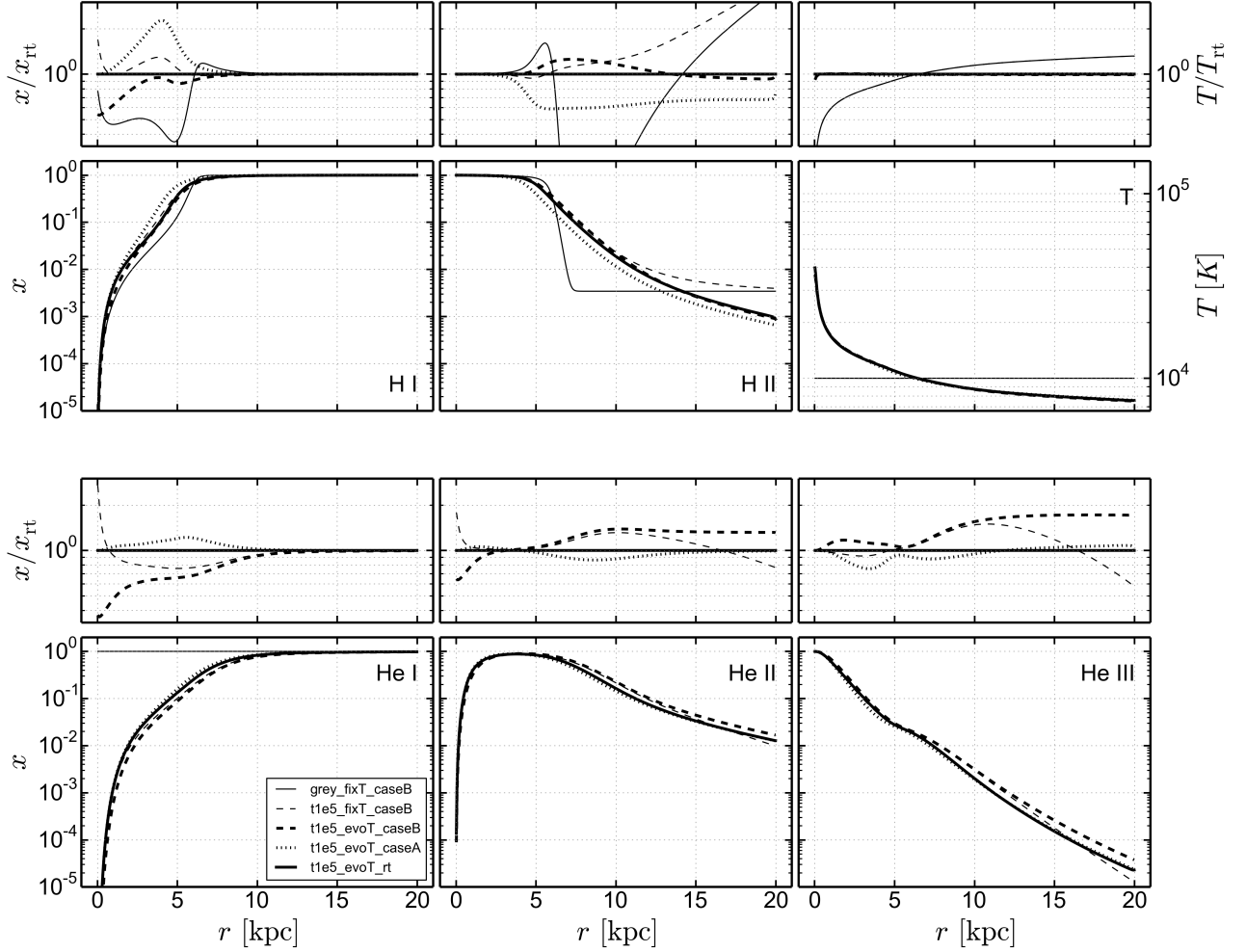


Figure 11: Ionization fraction and temperature profiles in five simple Strömgren sphere models. Each panel shows the ionization fraction of one ion or the temperature. The five models considered are: 1) **grey_fixT_caseB** (thin solid) in which the grey approximation to the 10^5 K blackbody spectrum is used, the temperature is kept fixed, and recombination rates are case B, 2) **t1e5_fixT_caseB** (thin dashed) in which the full 10^5 K blackbody spectrum is used, the temperature is kept fixed, and recombination rates are case B, 3) **t1e5_evoT_caseB** (thick dashed) in which the full 10^5 K blackbody spectrum is used, equilibrium temperatures are calculated, and recombination rates are case B, 4) **t1e5_evoT_A** (dotted) as in **t1e5_evoT_B** but with case A recombination rates (i.e. recombination radiation is ignored) and 5) **t1e5_evoT_rt** (thick solid) in which the full 10^5 K blackbody spectrum is used, equilibrium temperatures are calculated, recombination rates are case A, and recombination radiation is transferred through the system as opposed to being absorbed on the spot. Above each profile we show the ratio of each model's prediction to those of **t1e5_evoT_rt** (i.e. dex of difference in the profile panels). The scale in the top panels is a factor of three in either direction.

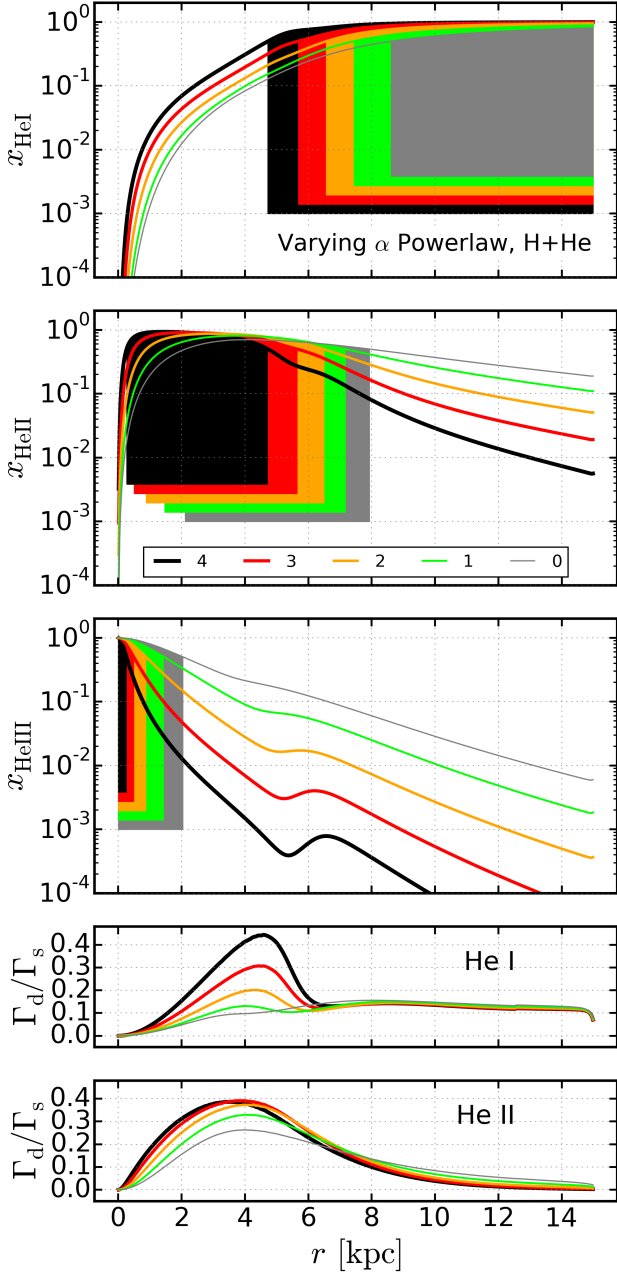


Figure 10: The effect of the powerlaw index, α , on the helium ionization structure. In the upper three panels we show the ionization fractions for neutral, singly ionized, and doubly ionized helium. We show the results for five power-law spectra, $L_\nu \propto \nu^{-\alpha}$, with α ranging between 4 and 0 (in black, red, orange, lime, and grey respectively). In each of these panels, the radii for which the ionization fraction is above 0.5 are indicated with a filled region. In the lower panels we show the ratio of diffuse to central source photo-ionization rates. As the spectrum becomes steeper, the contribution from recombination radiation becomes more important.

tion of each model's predictions to those of **t1e5_evoT_rt** (i.e. dex of difference in the bottom panel). By comparing models **grey_fixT_B** and **t1e5_fixT_B** we can isolate the effect of using the grey approximation. The monochromatic model is characterized by a steep transition from ionized to neutral hydrogen at approximately 7 kpc which can be seen clearly in the x_{HII} panel. As in the case of the slab, using the polychromatic thermal spectrum smooths the hydrogen ionization profile. We note that the two models reach the same x_{HII} value at large radii where collisional ionizations dominate over photo-ionizations for hydrogen. The harder photons that escape the ionized hydrogen region have a larger cross-section for absorption due to helium than from hydrogen.

By comparing models **t1e5_fixT_B** and **t1e5_evoT_B** we can isolate the effect of self-consistently calculating the temperature structure. The equilibrium temperature is greater than 10^4 K in the region in which hydrogen is ionized, but falls below that temperature at larger radii. For hydrogen, this produces lower neutral fractions at small radii and lower ionized fractions at large radii. This is because the ionization state of hydrogen at radii $r > 7$ kpc is determined by collisional ionizations. For helium, the higher temperatures at small radii also reduce x_{HeI} , but helium ionizing photons still reach radii where the temperature is cooler than 10^4 K and the reduced absorption of photons at small radii due to the higher temperatures leads to larger ionized fractions for both x_{HeII} and x_{HeIII} in model **t1e5_evoT_B**.

The larger case A recombination rate in model **t1e5_evoT_A** produces more neutral species for both hydrogen and helium. In model **t1e5_evoT_rt** we calculate the transfer of recombination photons isotropically emitted from each layer. As in the case of the slab, the rt and case A solutions agree in the optically thin center of the sphere. Interestingly, the case B approximation is more accurate for hydrogen while the case A approximation is more accurate for helium. Overall, the variations we have examined lead to differences of approximately a factor of 2 for the hydrogen ionization profiles and a factor of 50% for the helium ionization profiles.

8. Background Sphere Solver

In this section we describe the **SphereBgnd** class which models a spherically symmetric gas distribution placed in an isotropic background radiation field. Even in the simplified case of monochromatic radiation incident on a uniform density and temperature sphere, there are no analytic solutions for the ionization profile. In addition, the code we have used for comparison thus far, **CLOUDY**, does not support this geometry.

This geometry has been studied in the context of mini-halo evaporation (e.g. Shapiro et al., 2004) and in the context of hydrogen absorption systems (e.g. Zheng and Miralda-Escudé, 2002) however a direct comparison with either work would not be fruitful. In the first case, ionization profiles are not presented. In the second it would be difficult to know if differences arise from the set of included physical processes, the method of solution, or the implementation in code. Our goal for this final section is not a validation of the **SphereBgnd** class but rather a description of results in the light of the other validated pieces of

the **RABACUS**. A complete validation of this geometry must await a dedicated comparison project.

In what follows we will describe a simple model for a gaseous halo immersed in the cosmic UV background radiation. Dark matter halos have been shown to have universal density profiles (Navarro et al., 1997) characterized by a scale radius R_s . To model the gaseous component of the halo we create an NFW profile with a core at $r = 3R_s/4$ as in Maller and Bullock (2004) and Barnes and Haehnelt (2014). Specifically, the virial radius R_v is related to the virial mass M_v as,

$$R_v = 46.1 \text{ kpc} \left(\frac{\Delta_v \Omega_m h^2}{24.4} \right)^{-1/3} \left(\frac{1+z}{3.3} \right)^{-1} \left(\frac{M_v}{10^{11} M_\odot} \right)^{1/3} \quad (41)$$

where Δ_v is the mean overdensity inside the virial radius of the halo. The ratio of the virial radius and the scale radius is known as the concentration parameter $c = R_v/R_s$. For our simple model we take the average relationship between concentration and virial mass described in Macciò et al. (2007),

$$c = c_0 \left(\frac{M_v}{10^{11} M_\odot} \right)^{-0.109} \left(\frac{1+z}{4} \right)^{-1} \quad (42)$$

with $c_0 = 3.5$. The gaseous hydrogen density profile is,

$$n_H(r) = \frac{R_s^3 \rho_0}{[r + (3/4)R_s](r + R_s)^2} \quad (43)$$

where ρ_0 is a constant set such that the integrated hydrogen gas mass is equal to $M_H = f_H M_v$ and $f_H = (1 - Y_p)\Omega_b/\Omega_m$. The profile is then fully specified by choosing a virial mass, a mean overdensity inside the virial radius, and a redshift which we take to be $M_v = 10^{10} M_\odot$, $\Delta_v = 200$, and $z = 0$ for our example. This results in a concentration parameter of 18.

The ray tracing tools necessary to calculate the transfer of the isotropic background through the spherical geometry are the same we described in the context of isotropic recombination radiation. In other words, any ray we need to trace for treating an isotropic background can also, through the appropriate rotation, be made to be perpendicular to the vertical axis. In Fig. 12 we show ionization and temperature profiles using the same five models as in Fig. 3: **grey_fixT_B**, **hm12_fixT_B**, **hm12_evoT_B**, **hm12_evoT_A**, and **hm12_evoT_rt**. In this case, the steep density profile serves to lessen the differences between the models relative to the constant density slab case. This is partly due to the fact that the chosen halo mass produces a neutral core for all models. Models are most sensitive to changes when the core is near the optically thin to optically thick transition. Examining in detail the contribution to absorber abundances from different halo masses is beyond the scope of this paper, but one of the primary intended applications of **RABACUS**.

9. Conclusion

We have described **RABACUS**, a Python package for calculating the transfer of hydrogen ionizing radiation in simplified geometries relevant to astronomy and cosmology. We presented example solutions for: 1) a semi-infinite slab gas distribution

with isotropic radiation incident from both sides, 2) a spherically symmetric gas distribution with a point source at the center, and 3) a spherically symmetric gas distribution in a uniform background. We have also demonstrated the effects of temperature evolution, the inclusion of helium, and the treatment of recombination radiation on the ionization and temperature profiles in these geometries. For slabs exposed to isotropic backgrounds at Lyman limit system densities, these processes can change hydrogen and helium column densities by an order of magnitude. In the case of spherical geometries the magnitude of these effects is not as large but can still change ionization fractions by factors of 2. The flexibility and speed of **RABACUS** lend itself to rapid prototyping of ideas and allows it to serve as a check for more complicated radiative transfer schemes. It is made publicly available and is written in an interpreted language, Python, with a large user base. Future improvements will include the addition of metal line cooling and non-equilibrium solvers.

Acknowledgments

We thank an anonymous referee for an insightful review that helped improve this manuscript. JHW acknowledges support by NSF grants AST-1211626 and AST-1333360.

Appendix A. Recombination Radiation

In this section we examine in more detail the Stromgren sphere test described in §7.5. Our goal is to determine the total opacity encountered by recombination photons and the relative contribution to the total from different ions. We will make use of the quantity τ^r which is simply the optical depth through each thin radial shell of thickness dr ,

$$\begin{aligned} \tau_{13.6}^r/dr &= n_{\text{H}} \sigma_{\text{H}}(E_{\text{H}}) \\ \tau_{24.6}^r/dr &= n_{\text{H}} \sigma_{\text{H}}(E_{\text{H}}) + n_{\text{HeI}} \sigma_{\text{HeI}}(E_{\text{HeI}}) \\ \tau_{54.4}^r/dr &= n_{\text{H}} \sigma_{\text{H}}(E_{\text{HeII}}) + n_{\text{HeI}} \sigma_{\text{HeI}}(E_{\text{HeII}}) + n_{\text{HeII}} \sigma_{\text{HeII}}(E_{\text{HeII}}) \end{aligned} \quad (\text{A.1})$$

In Fig. A.13 we show the radial dependence of several quantities. The top panel shows the emission coefficients as calculated in Eqs. 37 and 38. The majority of recombination photons emitted at any radii come from hydrogen. At inner radii, recombinations of doubly ionized helium produce the majority of helium recombination photons while at radii greater than 5 kpc both types of helium recombination produce a similar number of photons.

In the middle three panels we show how the total opacity is partitioned amongst the absorbing species. Photons at 13.6 eV are only absorbed by hydrogen and so the optical depth profile follows that of the n_{H} profile (see bottom panel in the same figure). Photons at 24.6 eV are absorbed mostly by neutral hydrogen. The cross-section for absorption by helium is six times larger than that of hydrogen at this energy, but the greater density of neutral hydrogen at all radii more than compensates for this. Photons at 54.4 eV can be absorbed by all three absorbing species. The cross-sections at this energy for both helium

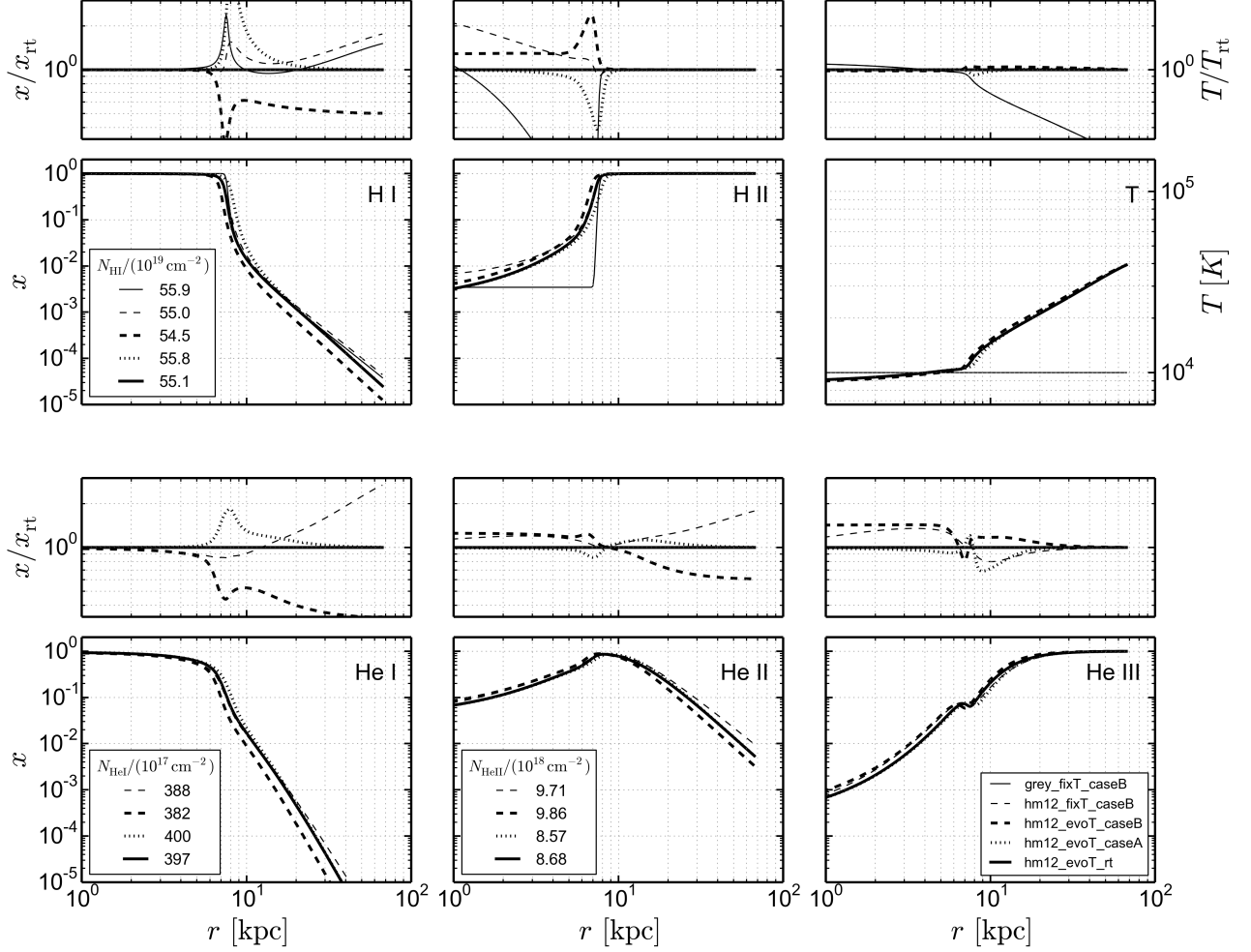


Figure 12: Ionization fraction and temperature profiles in five simple models of a gaseous halo in the UV background. Each panel shows the ionization fraction of one ion or the temperature. The five models considered are: 1) **grey_fixT_caseB** (thin solid) in which the grey approximation to the HM12 spectrum is used, the temperature is kept fixed, and recombination rates are case B, 2) **hm12_fixT_caseB** (thin dashed) in which the full HM12 spectrum is used, the temperature is kept fixed, and recombination rates are case B, 3) **hm12_evoT_caseB** (thick dashed) in which the full HM12 spectrum is used, equilibrium temperatures are calculated, and recombination rates are case B, 4) **hm12_evoT_A** (dotted) as in **hm12_evoT_B** but with case A recombination rates (i.e. recombination radiation is ignored), and 5) **hm12_evoT_rt** (thick solid) in which the full HM12 spectrum is used, equilibrium temperatures are calculated, recombination rates are case A, and recombination radiation is transferred through the system as opposed to being absorbed on the spot. Above each profile we show the ratio of each model's prediction to those of **hm12_evoT_rt** (i.e. dex of difference in the profile panels). The scale in the top panels is a factor of three in either direction.

species differ by less than ten percent, but singly ionized helium has a cross-section that is 13 times larger than that of hydrogen. At small radii, singly ionized helium absorbs the majority of photons. At larger radii, neutral hydrogen and helium absorb a similar amount of photons but the absorption by hydrogen is always equal to or greater than that by neutral helium. In Fig. A.14 we examine changes to the hydrogen ionization profile caused by the inclusion of helium in §7.5. There are two competing effects to consider. Helium will absorb some of the source photons that would have been absorbed by hydrogen, however some fraction of the helium recombination photons will be absorbed by hydrogen. In the bottom two panels of Fig. A.14 we show that the first is larger and that the neutral hydrogen fraction increases by as much as twenty percent when helium is included. Part of the reason that the helium photons do not make a larger contribution is because they escape the system. This can be seen in the top panel in which we show $\tau^{>r}$.

$$\begin{aligned}\tau_{13.6}^{>r} &= \int_r^\infty \tau_{13.6}^r \\ \tau_{24.6}^{>r} &= \int_r^\infty \tau_{24.6}^r \\ \tau_{54.4}^{>r} &= \int_r^\infty \tau_{54.4}^r\end{aligned}\quad (\text{A.2})$$

The optical depth to the surface of the sphere for photons at 54.4 eV is only larger than unity at radii smaller than 6 kpc. While recombination photons at 24.6 eV do encounter significant optical depth, the abundance of these photons is always lower than those from hydrogen recombinations (see top panel of Fig. A.13).

References

- Altay, G., Croft, R.A.C., Pelupessy, I., 2008. SPHRAY: a smoothed particle hydrodynamics ray tracer for radiative transfer. *MNRAS* 386, 1931–1946. 0802.3698.
- Altay, G., Theuns, T., 2013. URCHIN: a reverse ray tracer for astrophysical applications. *MNRAS* 434, 748–764. 1304.4235.
- Altay, G., Theuns, T., Schaye, J., Crighton, N.H.M., Dalla Vecchia, C., 2011. Through Thick and Thin - H I Absorption in Cosmological Simulations. *ApJ* 737, L37. 1012.4014.
- Barnes, L.A., Haehnelt, M.G., 2014. The bias of DLAs at $z \sim 2.3$: evidence for very strong stellar feedback in shallow potential wells. *MNRAS* 440, 2313–2321. 1403.1873.
- Cantalupo, S., Porciani, C., 2011. RADAMESH: cosmological radiative transfer for Adaptive Mesh Refinement simulations. *MNRAS* 411, 1678–1694. 1009.1625.
- Faucher-Giguère, C.A., Lidz, A., Zaldarriaga, M., Hernquist, L., 2009. A New Calculation of the Ionizing Background Spectrum and the Effects of He II Reionization. *ApJ* 703, 1416–1443. 0901.4554.
- Ferland, G.J., Porter, R.L., van Hoof, P.A.M., Williams, R.J.R., Abel, N.P., Lykins, M.L., Shaw, G., Henney, W.J., Stancil, P.C., 2013. The 2013 Release of Cloudy. *Rev. Mexicana Astron. Astrofis.* 49, 137–163. 1302.4485.
- Friedrich, M.M., Mellema, G., Iliev, I.T., Shapiro, P.R., 2012. Radiative transfer of energetic photons: X-rays and helium ionization in C²-RAY. *MNRAS* 421, 2232–2250. 1201.0602.
- Furlanetto, S.R., Stoever, S.J., 2010. Secondary ionization and heating by fast electrons. *MNRAS* 404, 1869–1878. 0910.4410.
- Haardt, F., Madau, P., 2012. Radiative Transfer in a Clumpy Universe. IV. New Synthesis Models of the Cosmic UV/X-Ray Background. *ApJ* 746, 125. 1105.2039.

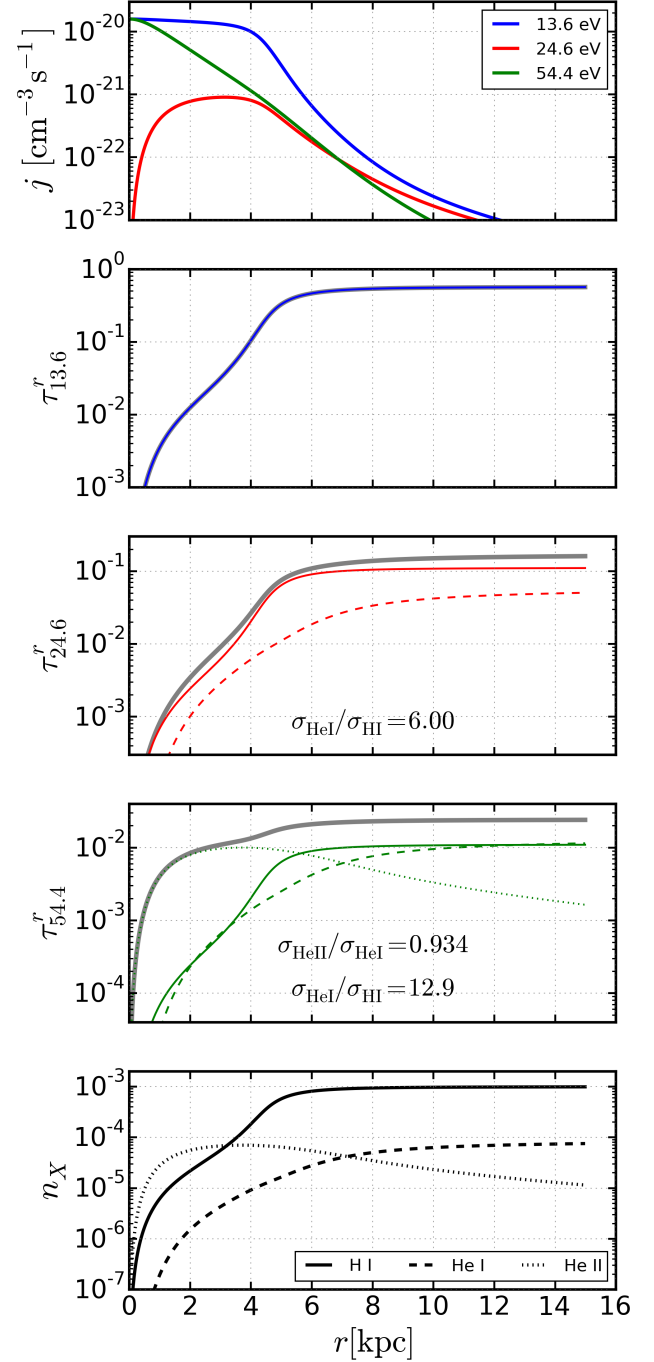


Figure A.13: The opacity encountered by recombination radiation in the Stromgren sphere test of in §7.5. The top panel shows the emission coefficients as calculated in Eqs. 37 and 38. The three middle panels show τ^r (see Eq. A.1) as a function of radius at the ionization energies of hydrogen and helium. The total τ^r (solid grey line) at each radius is the sum of contributions from neutral hydrogen, neutral helium and singly ionized helium (solid, dashed, and dotted lines respectively). The bottom panel shows the number density of each ion as a function of radius. Hydrogen absorbs the majority of recombination radiation at 13.6 eV and 24.6 eV. For recombination radiation at 54.4 eV, singly ionized helium absorbs the majority of photons at the inner radii while neutral hydrogen and helium absorb the majority at larger radii.

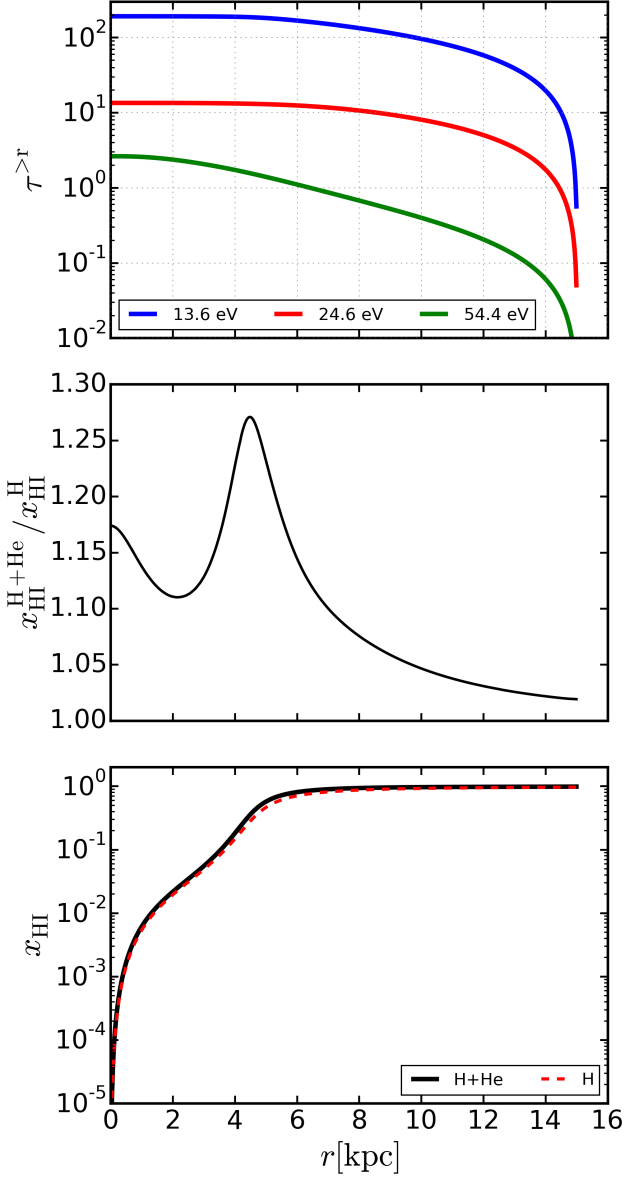


Figure A.14: The effect of helium on the ionization profile of hydrogen in the Stromgren sphere test in §7.5. In the top panel we show $\tau^{>r}$ (see Eq. A.2) for the three ionization threshold energies of hydrogen and helium. This can be used to understand how many recombination photons escape the system. In the bottom two panels we show the neutral hydrogen ionization fraction profile with and without helium. The inclusion of helium enhances x_{HI} by as much as 25%.

- Hollenbach, D.J., Tielens, A.G.G.M., 1999. Photodissociation regions in the interstellar medium of galaxies. *Reviews of Modern Physics* 71, 173–230.
- Hui, L., Gnedin, N.Y., 1997. Equation of state of the photoionized intergalactic medium. *MNRAS* 292, 27. [astro-ph/9612232](#).
- Iliev, I.T., Ciardi, B., Alvarez, M.A., Maselli, A., Ferrara, A., Gnedin, N.Y., Mellema, G., Nakamoto, T., Norman, M.L., Razoumov, A.O., Rijkhorst, E.J., Ritzerveld, J., Shapiro, P.R., Susa, H., Umemura, M., Whalen, D.J., 2006. Cosmological radiative transfer codes comparison project - I. The static density field tests. *MNRAS* 371, 1057–1086. [astro-ph/0603199](#).
- Macciò, A.V., Dutton, A.A., van den Bosch, F.C., Moore, B., Potter, D., Stadel, J., 2007. Concentration, spin and shape of dark matter haloes: scatter and the dependence on mass and environment. *MNRAS* 378, 55–71. [astro-ph/0608157](#).
- Maller, A.H., Bullock, J.S., 2004. Multiphase galaxy formation: high-velocity clouds and the missing baryon problem. *MNRAS* 355, 694–712. [astro-ph/0406632](#).
- McQuinn, M., Oh, S.P., Faucher-Giguère, C.A., 2011. On Lyman-limit Systems and the Evolution of the Intergalactic Ionizing Background. *ApJ* 743, 82. 1101.1964.
- Meiksin, A.A., 2009. The physics of the intergalactic medium. *Reviews of Modern Physics* 81, 1405–1469. 0711.3358.
- Navarro, J.F., Frenk, C.S., White, S.D.M., 1997. A Universal Density Profile from Hierarchical Clustering. *ApJ* 490, 493. [astro-ph/9611107](#).
- Planck Collaboration, Ade, P.A.R., Aghanim, N., Armitage-Caplan, C., Arnaud, M., Ashdown, M., Atrio-Barandela, F., Aumont, J., Baccigalupi, C., Banday, A.J., et al., 2013. Planck 2013 results. XVI. Cosmological parameters. *ArXiv e-prints* 1303.5076.
- Rahmati, A., Pawlik, A.H., Raičević, M., Schaye, J., 2013. On the evolution of the H I column density distribution in cosmological simulations. *MNRAS* 430, 2427–2445. 1210.7808.
- Raičević, M., Pawlik, A.H., Schaye, J., Rahmati, A., 2014. The effect of recombination radiation on the temperature and ionization state of partially ionized gas. *MNRAS* 437, 2816–2830. 1311.0182.
- Ritzerveld, J., 2005. The diffuse nature of Strömgren spheres. *A&A* 439, L23–L26. [astro-ph/0506637](#).
- Röllig, M., Abel, N.P., Bell, T., Bensch, F., Black, J., Ferland, G.J., Jonkheid, B., Kamp, I., Kaufman, M.J., Le Bourlot, J., Le Petit, F., Meijerink, R., Morata, O., Ossenkopf, V., Roueff, E., Shaw, G., Spaans, M., Sternberg, A., Stutzki, J., Thi, W.F., van Dishoeck, E.F., van Hoof, P.A.M., Viti, S., Wolfire, M.G., 2007. A photon dominated region code comparison study. *A&A* 467, 187–206. [astro-ph/0702231](#).
- Shapiro, P.R., Iliev, I.T., Raga, A.C., 2004. Photoevaporation of cosmological minihaloes during reionization. *MNRAS* 348, 753–782. [astro-ph/0307266](#).
- Shull, J.M., van Steenberg, M.E., 1985. X-ray secondary heating and ionization in quasar emission-line clouds. *ApJ* 298, 268–274.
- Strömgren, B., 1939. The Physical State of Interstellar Hydrogen. *ApJ* 89, 526.
- Verner, D.A., Ferland, G.J., Korista, K.T., Yakovlev, D.G., 1996. Atomic Data for Astrophysics. II. New Analytic FITS for Photoionization Cross Sections of Atoms and Ions. *ApJ* 465, 487. [astro-ph/9601009](#).
- Wiersma, R.P.C., Schaye, J., Smith, B.D., 2009. The effect of photoionization on the cooling rates of enriched, astrophysical plasmas. *MNRAS* 393, 99–107. 0807.3748.
- Wolfe, A.M., Gawiser, E., Prochaska, J.X., 2005. Damped Ly α Systems. *ARA&A* 43, 861–918. [astro-ph/0509481](#).
- Zheng, Z., Miralda-Escudé, J., 2002. Self-shielding Effects on the Column Density Distribution of Damped Ly α Systems. *ApJ* 568, L71–L74. [astro-ph/0201275](#).